



Optimization strategy of single-digit nanomolar cross-class inhibitors of mammalian and protozoa cysteine proteases

Lorenzo Cianni^{a,1}, Fernanda dos Reis Rocho^{a,1}, Fabiana Rosini^a, Vinícius Bonatto^a, Jean F.R. Ribeiro^a, Jerônimo Lameira^{a,b}, Andrei Leitão^a, Anwar Shamim^{a,*}, Carlos A. Montanari^{a,*}

^a Medicinal and Biological Chemistry Group, Institute of Chemistry of São Carlos, University of São Paulo, Avenue Trabalhador Sancarlene, 400, 23566-590 São Carlos, SP, Brazil

^b On Leave from Drug Designing and Development Laboratory, Federal University of Pará, Rua Augusto Correa S/N, Belém, PA, Brazil

ARTICLE INFO

Keywords:

Cysteine protease inhibitors
Structure activity relationships
Molecular dynamics simulation
Matched molecular pair analysis
Isothermal titration calorimetry
Differential scanning calorimetry

ABSTRACT

Cysteine proteases (CPs) are involved in a myriad of actions that include not only protein degradation, but also play an essential biological role in infectious and systemic diseases such as cancer. CPs also act as biomarkers and can be reached by active-based probes for diagnostic and mechanistic purposes that are critical in health and disease. In this paper, we present the modulation of a CP panel of parasites and mammals (*Trypanosoma cruzi* cruzain, LmCPB, CatK, CatL and CatS), whose inhibition by nitrile peptidomimetics allowed the identification of specificity and selectivity for a given CP. The activity cliffs identified at the CP inhibition level are useful for retrieving trends through multiple structure–activity relationships. For two of the cruzain inhibitors (**10g** and **4e**), both enthalpy and entropy are favourable to Gibbs binding energy, thus overcoming enthalpy–entropy compensation (EEC). Group contribution of individual molecular modification through changes in enthalpy and entropy results in a separate partition on the relative differences of Gibbs binding energy ($\Delta\Delta G$). Overall, this study highlights the role of CPs in polypharmacology and multi-target screening, which represents an imperative trend in the actual drug discovery effort.

1. Introduction

Currently, druggable cysteine proteases (CPs) are fundamental biological targets for the discovery of novel therapeutics for many human diseases: from parasitic diseases to cancer [1–4]. They are one of the most abundant classes of enzymes, being involved in many biological processes, such as cell-cycle, signaling, and cell death [2]. CatK is the only cathepsin expressed at high levels in osteoclasts. Thus, inhibitors have been developed for the treatment of bone diseases such as osteoporosis [5]. While CatL and CatS upregulations have been reported for many human cancers and autoimmune diseases, several inhibitors of these two enzymes are nowadays in clinical phase as new drug candidates [1,2].

Cruzain (Cz), also assigned as cruzipain (the full-length native enzyme), is the major cysteine protease expressed in the parasite *Trypanosoma cruzi*, which is the etiological agent of Chagas Disease (CD) [6]. Cz is present in all stages of the parasite life cycle, inducing damage to the host tissue and facilitating the parasite invasion.

Therefore, its inhibition interrupts several cellular processes leading to the death of the parasite [3].

LmCPB is one of the three families of CPs genes expressed in the genus *Leishmania*, along with the class A (LmCPA) and the class C (LmCPC) of cysteine proteases. The class B cysteine protease (CPB) is also part of the papain family and has essential involvement in the parasite life cycle in *L. mexicana* [4]. Accordingly, this enzyme is under investigation as a potential biological target for the treatment of diseases triggered by *L. mexicana* infection. Recently, we have disclosed an extrathermodynamic relationship to model the inhibition constants K_i , converted to the pK_i scale, between LmCPB and Cz. This quantitative model is useful for extracting chemical information that allows the prediction of structure–activity relationships (SARs) between the two enzymes [7].

In general, reversible inhibitors of mammalian CPs are mostly considered for the development of new drug candidates. A similar trend is observable for inhibitors of non-human cysteine proteases. The reason, in both cases, is to reduce *off-target* effects and thereby impair

* Corresponding authors.

E-mail addresses: shamim.hej@gmail.com (A. Shamim), Carlos.Montanari@usp.br (C.A. Montanari).

¹ these authors contributed equally to the work.

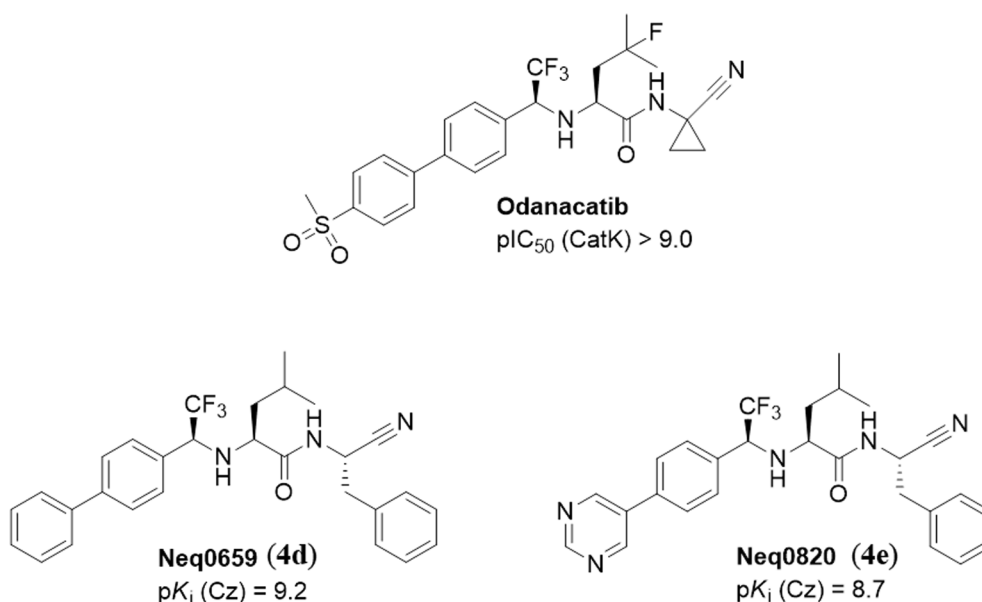


Fig. 1. 2D Structure representation of Odanacatib, Neq0659 (4d) and Neq0820 (4e) as high-affinity cysteine protease inhibitors.

undesirable reactions with endogenous nucleophiles and cytotoxicity [1].

We have recently reported that peptidic and non-peptidic nitrile based Cz inhibitors are efficient trypanocidal agents [7–10]. Specifically, we have conveyed on two new Odanacatib [11] derivatives (Neq0659 and Neq0820, numbered in this work as 4d and 4e) as low nanomolar Cz inhibitors, Fig. 1. We have also shown that the dipeptidyl nitrile scaffold tolerates S3-P3 interactions that can efficiently increase the affinity for the desired CP [12,13]. Thereafter, we have performed structural optimization, synthesis and structure–activity relationships (SARs) on a panel of CPs (Cz, LmCPB, CatK, CatL and CatS) for nitrile-based inhibitors by the deconstruction of our published inhibitors (Neq0659 and Neq0820, numbered in this work as 4d and 4e). To better understand the reasons for cross-class inhibition of the new inhibitors described here, we performed molecular dynamics simulations (MDS), isothermal titration calorimetry (ITC) and differential scanning calorimetry (DSC) studies on Cz inhibitors as CP surrogates.

2. Methods

2.1. Molecular dynamics simulations

Herein, the initial coordinates for molecular dynamics simulations were taken from CatS crystal structure with PDB code 3OVX [14] and Cz crystal structure with PDB code 3I06 [15]. Note that ligands were placed in the active site of CatS and Cz using the coordinate information obtained from the crystal structure of a dipeptidyl nitrile in complex with Cz [9]. The partial charges for ligands were obtained using AM1-BCC [16] and the ligands were parameterized with the GAFF [16] force field. Each system was solvated in a truncated octahedron TIP3P water box [17]. Counter ions were added to maintain the electro-neutrality of each ligand–protein complex system. It is also important to point out that the standard protonation state at pH = 7 was assigned to all ionizable residues, where the protonation states of all the residues of protein were carefully defined according to the PROPKA [17]. The AMBER 16 suite of programs [18] together with the Amber ff14SB [19] force field were used to perform MD simulations, where the SHAKE algorithm [20] was used to maintain all the bonds at their equilibrium distances. Initially, the hydrogen atoms, water molecules, and ions were minimized using 10,000 cycles of steepest descent and conjugate gradient algorithms. Then, the whole system was heated through several

heating steps. Finally, we performed 100 ns of MD simulation using the NPT ensemble for each ligand–CatS non-covalent complex and ligand–Cz covalent complexes. To analyze all the MD trajectories, we have used CPPTRAJ [21] available in AmberTools software package. The fluctuation graphs were produced through GnuPlot 5.0 [22]. We used Chimera (UCSF) [23] to visualize the output of the simulations and generate the Figures related to the computational results.

2.2. Synthesis

All chemicals were purchased as reagent grade and used without further purification, unless otherwise noted. *N,N*-Dimethylformamide (DMF) was dried over 3 Å activated molecular sieves for 72 h. All non-aqueous reactions were carried out under argon atmosphere in oven-dried glassware. Solvents used in high performance chromatography (HPLC) were supplied by Tedia and used without further purification.

Thin layer chromatography was performed on Fluka Analytical Sigma-Aldrich silica gel matrix, pre-coated plates with fluorescent indicator 254 nm and/or staining solutions. Flash column chromatography was performed on silica gel (pore size 60 Å, 70–230 mesh).

¹H and ¹³C NMR spectra were recorded on HP – 400 and 500 MHz instruments in CDCl₃ or DMSO-*d*₆. Chemical shifts are referenced to the residual solvent peak and J values are given in Hz. The following multiplicity abbreviations are used: (s) singlet, (d) doublet, (dd) doublet of doublets, (ddd) doublet of doublet of doublets, (dt) doublet of triplet, (t) triplet, (q) quartet, (m) multiplet, and (br) broad.

Characterization and separation of compounds were carried out with a HPLC system. The analytical HPLC system consisted of a Shimadzu LC (Kyoto, Japan) equipped with a LC-20AT pump, a LC-20AD pump, a SIL-20A HT autosampler, a DGU-20A5 degasser, a CBM-20A, SPD-M20A DAD detector and an FRC-10A fraction collector. Data acquisition was performed using LCsolution software version 1.26 SP5. The LC system was coupled to an AmaZon SL ion trap mass spectrometer (Bruker Daltonics, Bremen, Germany) equipped with an electrospray ionization (ESI) interface. Data acquisition was performed with Bruker Daltonics Data Analysis software (version 4.2.383.1). Spectra for all compounds and further details can be found in the supplementary information.

Solvents were filtered through a 0.45 µm Merck-Millipore filter before use and degassed in an ultrasonic bath. In the established HPLC protocol, chiral analysis and separation were carried out at 32 °C (column oven) where not otherwise specified, using analytical and

semi-preparative cellulose-2 Phenomenex column (Analytical: 5 μm , 250 mm \times 4.6 mm I.D., semi-preparative: 5 μm , 250 mm \times 10 mm I.D.) or Diacel column (IC-chiralpak: 5 μm , 250 mm \times 4.6 mm) via isocratic elution with a flow rate of 0.5 (analytical) and 2.36 mL min⁻¹ (semi-preparative). The most common mobile phase composition was acetonitrile–water (50:50) (v/v). Volumes of 10 μL (analytical) and 1000 μL (semi-preparative) were injected. Quantification was carried out at 200–800 nm and the chromatographic run time varied according to the sample.

Specific rotations ($[\alpha]^T = 100 \alpha/\text{lc}$, in deg mL g⁻¹ dm⁻¹, but reported herein in degrees) were observed at the wavelength 589 nm, the D line of a sodium lamp. T was set to be 25 °C. Samples were weighted using a precision balance (Sartorius, Model CPA26P) and dissolved in methanol (HPLC grade, PanReac). Rotations were measured using a Digital Polarimeter (P2000, Jasco): α = observed rotation in degrees; l = cell path length of 0.1 decimeter; c = concentration in g 100 mL⁻¹. Values were calculated using 5 measurements for each compound. Melting points were determined by a Quimica Micro MQAPF-302 apparatus and are uncorrected.

2.2.1. General procedure for the synthesis of amines from ketones and aminoacids (GP1)

To a solution of L-phenylalanine/L-leucine methylester hydrochloride (1 mmol, 1 equiv.) in dry methanol (11 mL), under argon atmosphere, potassium carbonate (1.2 mmol, 1.2 equiv.) and 3/4-bromo-2,2,2-trifluoroacetophenone (1.1 mmol, 1.1 equiv.) were added. The mixture was stirred at 50 °C for 18 h, then it was filtered to remove potassium carbonate and the solvent was evaporated to get white or slightly yellow gummy solid. The residue was used for the next step without further purification. The imine intermediate in a round bottom flask under argon was solubilized in MeOH then ACN was added. The temperature was decreased to -40 °C before adding freshly synthesized Zn(BH)₄ drop wise. The reaction was stirred for 3 h at -40 °C. After that, water was added drop wise until the bubbling stops. 2 M HCl was added until pH = 2. Then the mixture was extracted with ethyl acetate (3 \times 15 mL). The combined organic phases were dried over Na₂SO₄, filtered and evaporated under reduced pressure. The product was then purified by flash silica column chromatography using 20–30% ethyl acetate in hexane to get a white solid (55–60% yield over 2 steps).

2.2.2. General procedure for the synthesis of peptide bond (GP2)

The amine synthesized via GP1 (0.7 mmol, 1.0 equiv.). HATU (0.875 mmol, 1.25 equiv.) and (S)-2-amino-3-phenylpropanenitrile (0.79 mmol, 1.1 equiv.) were sequentially introduced into a 25 mL round bottomed reaction flask, provided with magnetic stirrer and under argon atmosphere. Then, dry DMF (7 mL) and N,N-diisopropylethylamine (1.75 mmol, 2.5 equiv.) were added. After 22 h at room temperature, ethyl acetate (30 mL) was added to the reaction and the organic layer was washed with saturated aqueous NaHCO₃ (3 \times 20 mL) and Brine (3 \times 20 mL). The organic layer was dried over Na₂SO₄, filtered and dried under reduced pressure. Purification by flash column chromatography on silica (ethyl acetate: n-hexane 2:8 v/v) gave the peptide as a white solid (60–70% yield).

2.2.3. General procedure for the synthesis of C–C bond via suzuki reaction (GP3)

A stream of argon was passed through a suspension of aryl bromide **3e** (0.43 mmol, 1.0 equiv.) synthesized via GP1 followed by GP2, the proper aryl/heteroaryl boronic acid (0.56 mmol, 1.3 equiv.), 2 M Na₂CO₃ (1.52 mL) and DMF (5 mL) for 10 min. PdCl₂(dppf) (5 mol %) was then added and the reaction was warmed to 80 °C and stirred under argon. After 3 h, H₂O (15 mL) was added and the aqueous phase was extracted with ethyl acetate (3 \times 15 mL). The combined organic phases were dried over Na₂SO₄ and purified by flash column chromatography using a gradient of ethyl acetate/n-hexane (3:7 to 8:2) to give a light yellow or white solid with a 50–75% yield. Final compounds were

purified by HPLC equipped with a chiral column.

2.2.4. Synthesis and characterization

Synthesis and characterization of compounds **3a–3c**, **4d** and **4e** are reported in our previous work [8].

(S)-N-((S)-1-cyano-2-phenylethyl)-3-phenyl-2-(((S)-2,2,2-trifluoro-1-phenylethyl)amino)propanamide **3d**. Compound **3d** was synthesized according to procedure GP1 followed by GP2 as a white solid (48.7% yield over 3 steps); mp. 99.0–99.7 °C. Purity (HPLC) > 99%. ¹H NMR (500 MHz, CDCl₃) δ 7.47–7.28 (m, 9H), 7.22 (d, J = 7.1 Hz, 2H), 7.18–7.11 (m, 4H), 5.02 (dt, J = 8.7, 6.5 Hz, 1H), 3.93 (q, J = 6.5 Hz, 1H), 3.43 (d, J = 5.4 Hz, 1H), 3.00 (dddd, J = 27.3, 20.7, 13.9, 6.0 Hz, 4H), 2.15 (s, 1H). ¹³C NMR (125 MHz, CDCl₃) δ 171.72, 135.91, 133.55, 132.46, 129.65, 129.36, 129.35, 129.06, 129.04, 129.00, 128.58, 128.03, 127.53, 124.89 (q, J = 282.2 Hz), 117.59, 63.30 (q, J = 28.7 Hz), 60.04, 40.90, 38.61, 37.46. IR (film, cm⁻¹) 3330.92, 3064.19, 3031.24, 2929.21, 2858.11, 2858.11, 2244.41, 1678.51, 1603.65, 1495.33, 1455.18, 1369.25, 1347.12, 1265.44, 1166.91, 1119.58, 1029.88, 918.63, 848.58, 746.17, 700.45. $[\alpha]_D^{23}$ (Chloroform) –468.33.

(S)-2-(((S)-1-(3-bromophenyl)-2,2,2-trifluoroethyl)amino)-N-((S)-1-cyano-2-phenylethyl)-4-methylpentanamide **3e**. Compound **3e** was synthesized according to procedure GP1 followed by GP2 as a white solid (50% yield over 3 steps); mp. 171.9–172.8 °C. Purity (HPLC) 97%. ¹H NMR (500 MHz, CDCl₃) δ 7.53 (ddd, J = 8.0, 1.8, 0.9 Hz, 1H), 7.43 (s, 1H), 7.39–7.32 (m, 3H), 7.27–7.16 (m, 4H), 6.96 (d, J = 5.7 Hz, 1H), 5.04 (dd, J = 15.5, 6.8 Hz, 1H), 3.93 (q, J = 6.9 Hz, 1H), 3.39 (dd, J = 8.3, 5.0 Hz, 1H), 3.11–2.96 (m, 2H), 1.69 (dt, J = 12.9, 6.5 Hz, 1H), 1.50 (ddd, J = 13.7, 8.6, 5.0 Hz, 1H), 1.36 (ddd, J = 14.2, 8.7, 5.8 Hz, 1H), 0.92 (dd, J = 6.3, 5.8 Hz, 6H). ¹³C NMR (126 MHz, CDCl₃) δ 172.77, 135.50, 133.62, 132.72, 131.22, 130.66, 129.30, 129.01, 128.04, 127.02, 126.34, 123.54, 122.96, 117.72, 63.16, 62.87, 62.58, 62.29, 59.55, 42.33, 40.87, 38.70, 24.78, 22.93, 21.75. IR (film, cm⁻¹) 3319.50, 3030.41, 2959.80, 2928.35, 2872.20, 2249.01, 1672.25, 1568.38, 1519.56, 1477.32, 1469.41, 1356.40, 1318.68, 1268.36, 1233.84, 1196.91, 1179.41, 1168.11, 1155.61, 1124.17, 1075.59, 921.49, 897.93, 875.32, 793.05, 718.47, 701.90. $[\alpha]_D^{23}$ (Chloroform) –158.73.

(S)-2-(((S)-1-([1,1'-biphenyl]-3-yl)-2,2,2-trifluoroethyl)amino)-N-((S)-1-cyano-2-phenylethyl)-4-methylpentanamide **4a**. Compound **4a** was synthesized according to procedure GP1 followed by GP2 and GP3 as a white gummy solid (31.1% yield over 4 steps). Purity (HPLC) 97%. ¹H NMR (500 MHz, CDCl₃) δ 7.66–7.55 (m, 3H), 7.52–7.43 (m, 3H), 7.39 (t, J = 7.4 Hz, 1H), 7.34–7.25 (m, 3H), 7.23 (d, J = 7.6 Hz, 1H), 7.18 (d, J = 6.5 Hz, 2H), 7.06 (d, J = 8.7 Hz, 1H), 5.02 (dt, J = 8.7, 6.8 Hz, 1H), 4.06 (dd, J = 9.6, 4.6 Hz, 1H), 3.46–3.34 (m, 1H), 3.06–2.93 (m, 2H), 2.06 (s, 1H), 1.79–1.68 (m, 1H), 1.53 (ddd, J = 13.7, 8.8, 4.8 Hz, 1H), 1.38 (ddd, J = 14.2, 8.8, 5.6 Hz, 1H), 0.93 (dd, J = 12.3, 6.6 Hz, 6H). ¹³C NMR (126 MHz, CDCl₃) δ 173.37, 142.10, 140.31, 134.28, 133.68, 129.52, 129.27, 129.01, 128.95, 128.89, 128.77, 128.27, 127.95, 127.71, 127.24, 127.06, 127.00, 126.52, 124.27, 122.02, 117.79, 63.76, 63.53, 63.30, 63.08, 59.26, 42.55, 40.91, 38.77, 24.83, 23.04, 21.78. IR (film, cm⁻¹) 3326.75, 3063.09, 3032.71, 2957.93, 2931.54, 2871.00, 2244.44, 1664.38, 1600.29, 1496.12, 1480.88, 1455.80, 1367.40, 1345.77, 1261.58, 1154.37, 1116.89, 851.91, 801.88, 757.65, 699.22. $[\alpha]_D^{23}$ (Chloroform) –173.00.

Synthesis of (S)-N-((S)-1-cyano-2-phenylethyl)-4-methyl-2-(((S)-2,2,2-trifluoro-1-(3',4',5'-trimethoxy-[1,1'-biphenyl]-3-yl)ethyl)amino)pentanamide **4b**. Compound **4b** was synthesized according to procedure GP1 followed by GP2 and GP3 as a white solid (33.1% yield over 4 steps); mp. 50.9–51.6 °C. Purity (HPLC) 97%. ¹H NMR (500 MHz,

CDCl_3) δ 7.57 (d, $J = 8.2$ Hz, 1H), 7.43 (dd, $J = 12.5, 4.6$ Hz, 2H), 7.34 – 7.26 (m, 3H), 7.23 (d, $J = 7.7$ Hz, 1H), 7.16 (d, $J = 6.3$ Hz, 2H), 7.04 (d, $J = 8.8$ Hz, 1H), 6.76 (s, 2H), 5.00 (dt, $J = 8.7, 6.9$ Hz, 1H), 4.05 (dd, $J = 8.7, 4.4$ Hz, 1H), 3.92 (d, $J = 10.9$ Hz, 9H), 3.45 – 3.39 (m, 1H), 2.93 (dd, $J = 7.7, 4.9$ Hz, 2H), 2.10 (s, 1H), 1.74 (ddd, $J = 12.7, 8.6, 6.5$ Hz, 1H), 1.51 (ddd, $J = 13.7, 8.8, 4.8$ Hz, 1H), 1.38 (ddd, $J = 9.9, 8.9, 5.6$ Hz, 1H), 0.94 (t, $J = 6.6$ Hz, 6H). ^{13}C NMR (126 MHz, $\text{DMSO}-d_6$) δ 174.91, 153.60, 140.69, 137.61, 136.08, 135.63, 135.45, 129.50, 128.90, 127.73, 127.20, 119.06, 104.69, 62.99 (q, $J = 20.0$ Hz), 60.63, 59.88, 56.40, 42.80, 41.85, 37.44, 24.58, 23.00, 22.45. IR (film, cm^{-1}) 3324.80, 2956.12, 2928.74, 2870.00, 2854.12, 1681.95, 1579.17, 1710.87, 1485.75, 1464.15, 1406.05, 1346.16, 1251.30, 1156.50, 1122.58, 1005.52, 796.58, 701.20. $[\alpha]_D^{23}$ (Chloroform) –192.31.

Synthesis of (2S)-N-(1-cyano-2-phenylethyl)-4-methyl-2-[[[(1S)-2,2,2-trifluoro-1-[3-(pyrimidin-5-yl)phenyl]ethyl]amino]pentanamide 4c. Compound **4c** was synthesized according to procedure GP1 followed by GP2 and GP3 as a white solid (36.1% yield over 4 steps); mp. 50.1–50.9 °C. Purity (HPLC) 97%. ^1H NMR (500 MHz, CDCl_3) δ 9.23 (s, 1H), 8.93 (s, 2H), 7.61 – 7.55 (m, 1H), 7.52 (t, $J = 7.7$ Hz, 1H), 7.43 (s, 1H), 7.38 – 7.25 (m, 4H), 7.22 – 7.18 (m, 2H), 7.11 (d, $J = 9.0$ Hz, 1H), 5.07 (dt, $J = 9.0, 6.6$ Hz, 1H), 4.05 (q, $J = 7.1$ Hz, 1H), 3.42 (dd, $J = 8.9, 4.8$ Hz, 1H), 3.00 (d, $J = 6.6$ Hz, 2H), 1.81 – 1.68 (m, 1H), 1.51 (ddd, $J = 13.7, 8.8, 4.8$ Hz, 1H), 1.39 (ddd, $J = 14.2, 8.9, 5.7$ Hz, 1H), 0.94 (dd, $J = 6.6, 4.2$ Hz, 6H); ^{13}C NMR (126 MHz, CDCl_3) δ 173.21, 157.63, 154.99, 135.31, 135.12, 133.66, 130.20, 129.35, 129.30, 129.01, 128.99, 128.95, 128.69, 128.11, 127.96, 126.96, 126.37, 125.24 (q, $J = 283.1$ Hz), 124.12, 117.82, 63.37 (q, $J = 28.8$ Hz), 59.73, 42.77, 40.74, 38.83, 24.82, 23.04, 21.72; IR (film, cm^{-1}) 3324.95, 3032.18, 2957.88, 2933.10, 2870.90, 2243.47, 1681.52, 1555.68, 1496.55, 1455.64, 1408.70, 1367.80, 1348.16, 1262.88, 1155.91, 1119.45, 1029.72, 798.06, 725.42, 700.93; $[\alpha]_D^{23}$ (Chloroform) –355.00.

Synthesis and characterization of compounds **10a** and **10b** and **10c**–**10k** are reported in our previous works [9] and [7], respectively.

2.3. Enzymatic inhibition studies

Expression, purification of Cruzain and LmCPB are reported in our recent works [13,24]. CatL, CatK and CatS were purchased by Enzo Life Science®.

2.3.1. Determination of the Michaelis constant (K_M)

The enzymatic kinetics assays were performed in fluorimeter equipment of the Biotek Synergy HT system, using a black 96-well microplate. (Corning®) at 37 °C. The excitation wavelength used was 360 nm and emission 460 nm. The enzymes were activated in an assay buffer (Table 1), containing 7 mM DTT (Sigma-Aldrich), and 0.014% of Triton X-100 (Sigma-Aldrich). The activation time and temperature vary between the enzymes. The concentrations used for the enzymes are shown in Table 1. The reaction rate was followed by 5 min, at which the hydrolysis rate of the fluorogenic substrate was measured. A final concentration of 5% (10 μL) of DMSO (Sigma-Aldrich) was used in each well. Eight different substrate concentrations were prepared with a 0.5 dilution factor. The assays were performed in triplicates and the results are shown in Table 2.

Table 1

Parameters used in kinetic assays for different cysteine proteases.

Enzyme	[Enzyme] (nM)	Substrate	Assay Buffer	Activation Time	Temperature of Activation
Cruzain	0.15	Z-FR-AMC	100 mM sodium acetate pH 5.5	15 min	0 °C
LmCPB	7.0	Z-FR-AMC	100 mM sodium acetate pH 5.5	15 min	0 °C
CatK	0.15	Z-LR-AMC	100 mM sodium acetate pH 5.5	30 min	37 °C
CatL	1.9	Z-FR-AMC	100 mM sodium acetate pH 5.5	20 min	0 °C
CatS	1.12	Z-FR-AMC	100 mM sodium citrate pH 6.0	60 min	37 °C

Table 2

K_M and V_{\max} obtained for the five CPs through the Michaelis-Menten equation. The experimental K_M results retrieved from BRENDA [25] website are: Cz, 1 to 3 μM ; LmCPB, 5 to 17 μM ; CatL, 0.7 to 6 μM ; CatS, 14 to 42 μM ; CatK, 1.5 to 4.6 μM .

Enzyme	K_M (μM)	V_{\max} ($\mu\text{mol g}^{-1} \text{s}^{-1}$)	k_{cat} (s^{-1})	k_{cat}/K_M ($\text{M}^{-1} \text{s}^{-1}$)
Cruzain	1.8 ± 0.2	7.4 ± 0.6	0.2 ± 0.01	11.1×10^4
LmCPB	6.7 ± 0.9	81 ± 8.5	2.1 ± 0.22	31.3×10^4
CatL	3.3 ± 0.2	11 ± 0.8	0.3 ± 0.02	9.1×10^4
CatS	37 ± 0.5	4.6 ± 1.5	0.1 ± 0.04	0.3×10^4
CatK	1.7 ± 0.07	2.2 ± 0.7	0.06 ± 0.01	3.5×10^4

2.3.2. Determination of the inhibition constant (K_i)

The enzymatic activity was evaluated by fluorimetric assays (Biotek Synergy HT), monitoring the hydrolysis rate of the fluorogenic substrate with fluorescence emission at 460 nm (excitation at 355 nm) at 37 °C. The same protocol described in Table 1 was used for the enzyme activation and concentration steps. The concentration of the substrates used in the assays was fixed and kept equal to the K_M value, so $[S] = K_M$.

Visual inspection and a pre-reading of the plate wells were carried out to check for possible precipitations and background fluorescence, respectively. None of the compounds showed a significant fluorescence signal at around 460 nm, the emission wavelength used to monitor the kinetics of the reaction. Thus, the potential effects of the inner-filter did not need to be considered in our experiments. Data analysis and manipulation were performed using Sigma Plot10.

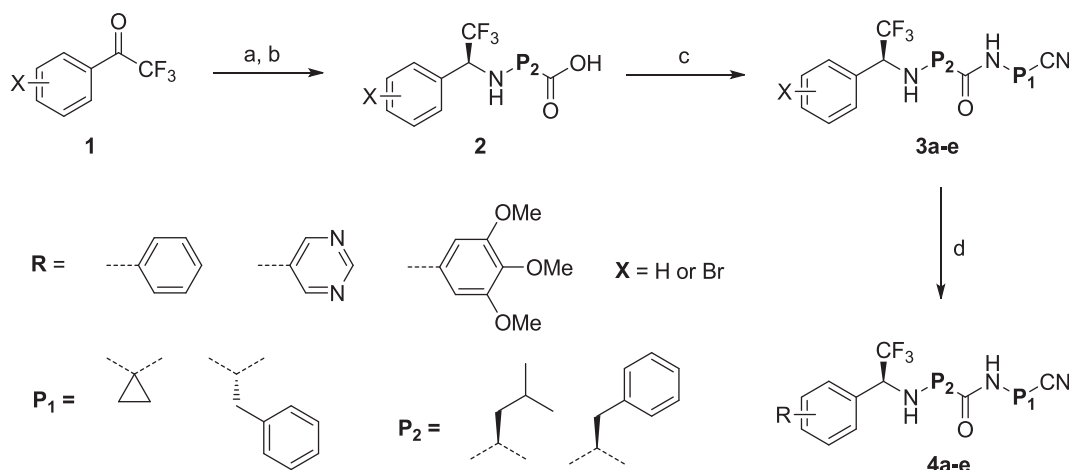
Each experiment was performed in triplicate for each compound. The initial rates of substrate hydrolysis under the first order reaction were calculated using the Gen5TM Biotek software. The apparent inhibition constant K_i' was determined by non-linear regression fit using the equation $V_s = V_o/(1 + [I]/K_i')$, where V_s is the steady-state rate, V_o is the rate in the absence of inhibitor, and $[I]$ is the inhibitor concentration. The true inhibition constant K_i was calculated by the correction of K_i' according to $K_i = K_i'/(1 + [S]/K_M)$, where $[S]$ is the substrate concentration and K_M is the Michaelis constant. A control measurement with the Neq0570 reversible covalent fast-binding inhibitor was performed for each configuration plate [13].

2.4. Isothermal titration calorimetry (ITC)

Dialysis and concentration were performed over 30 to 60 min period on Amicon ultra 10 kDa membranes (Merck Millipore). The inhibitor was placed in the syringe and the protein in the cell. 0.001% Triton-X 100 was added to the solution of the syringe and the cell to prevent the protein from aggregation. All thermodynamic parameters were calculated by Microcal PEAQ-ITC Analysis Software and experiments were performed at least in duplicate. The parameters were calculated using an appropriate one site fitting to model a cruzain one binding site. More details are reported in our previous work [13].

2.5. Differential scanning calorimetry (DSC)

The thermal stability assay was carried out for cruzain. The T_m ,



Scheme 1. General synthesis for compounds **3a-3e** and **4a-e**. Reagents and conditions: a) $\text{HCl} \cdot \text{H}_2\text{N}-\text{P}_2-\text{CO}_2\text{Me}$, K_2CO_3 , MeOH, 50 °C, 18 h; b) 1 M $\text{Zn}(\text{BH}_4)_2$ in DME, ACN/MeOH, -40 °C, 3 h; c) $\text{H}_2\text{N}-\text{P}_1-\text{CN}$, HATU, DIPEA, DMF, r.t., 7–20 h; d) aryl/heteroaryl boronic acid, PdCl_2dppf , Na_2CO_3 , DMF, 80 °C, 3 h.

temperature in which half of the protein is in the folded and unfolded form, was determined along with the ΔH_{TM} . The experiment was performed in a differential scanning calorimetry- Nano DSC of the TA Instruments. The instrument consists of two cells with a 600 μL of capacity, being one for the sample solution and the other for the reference.

2.5.1. Cruzain reversible assay

Cruzain was thawed at room temperature for approximately 5 min. After that, the protein was added in a dialysis membrane (Amicon Ultra) of 15 mL and 10 kDa, along with a buffer solution of 100 mM sodium acetate, 300 mM of NaCl and 5 mM of EDTA pH 5.5 and 1 mM of β -mercaptoethanol (Sigma-Aldrich). The solution was centrifuged (Eppendorf 5804R) at 4500 rcf at 4 °C for 35 min. Afterward, the solution was transferred to a micro centrifuge tube and kept on ice. The Cz concentration was measured in mg mL^{-1} using a DeNovixDS-11⁺ spectrometer; the measurement was repeated three times.

The samples for the reversibility assay were prepared with a final volume of 1000 μL . The sample solution was prepared with a Cz concentration of 30 μM (0.7 mg mL^{-1}), acetate buffer pH 5.5, 0.014% v/v of Triton X-100, and 5% of DMSO. The reference cell was prepared with the acetate buffer pH 5.5, 0.014% v/v of Triton X-100, and 5% of DMSO. Both samples were degassed for 5 min before being added to the equipment cells.

The experiment was performed with sequential scans at 3 atm and with a rate of 2 °C/min. First, the sample was heated from 0 to 90°, then it was cooled to 0 °C and again heated to 90 °C. The experiment was performed in duplicates.

2.5.2. Thermal stability of cruzain with different ligands

The dialysis of the protein was made in the same way described before. The samples were prepared with a final volume of 1000 μL . The sample solution was prepared with a Cz concentration of 30 μM (0.7 mg mL^{-1}), acetate buffer pH 5.5, 0.014% v/v of Triton X-100, 5% of DMSO and with a ligand concentration of 120 μM . The reference cell was prepared with the acetate buffer pH 5.5, 0.014% v/v of Triton X-100, and 5% of DMSO. Both samples were degassed for 5 min before being added to the equipment cells.

The blank was made for all the compounds, where the protein was removed from the sample cell. The experiment was performed in duplicates.

The experiment was performed with a single scan at 3 atm and with a rate of 2 °C/min, where the samples were heated, ranging from 0 °C to 90 °C.

3. Results and discussion

3.1. Design, synthesis, structure activity relationships (SARs) and molecular dynamics simulations

In a previous work, we performed an analysis of structure–activity relationships (SARs) for nitrile-based Cz inhibitors that incorporate a P2 amide replacement based on trifluoroethylamine (derivatives of Odanacatib, Fig. 1). Results unearthed two potent and selective inhibitors of Cz (**Neq0659** and **Neq0820**, here numbered as **4d** and **4e**) [8]. We observed a strong non-additive effect when inverting the configuration of the P3 substituent and inserting benzyl at P1. Therefore, we designed and synthesized four new derivatives (**3e**, **4a-4c**) of **Neq0659** and **Neq0820** that bear a *meta* substituent in P3 to evaluate the influence of the P3/S3 interaction in the bimolecular recognition process with different CPs. In fact, lately we leveraged the affinity of dipeptidyl nitrile inhibitors against Cz and CatL by a single atom substitution in *meta* position of their P3 phenyl ring [12,13]. The general synthesis of nitrile-based inhibitors bearing a trifluoroethylamine in P2 (**3a-3e** and **4a-4e**) is described in Scheme 1 and chemical structures are depicted in Fig. 2.

For a comprehensive approach to SARs, we included our *in-house* synthesized dipeptidyl nitrile inhibitors (**10a-10k**), whose binding affinities (pK_i) for a panel of CPs were published later [7]. The general synthesis of compounds **10a-10k** is reported in Scheme 2 and their chemical structures in Fig. 3.

The inhibition constants scaled to pK_i values were determined for parasite cysteine proteases (Cz, *Lm*CPB) and for human cysteine cathepsins (CatK, CatL, CatS) and are reported in Table 3. Compounds **10a** and **10c** have previously been described as competitive inhibitors by reversible binding to Cz [9]. Several new compounds are low nanomolar inhibitors for most of the CPs now reported. The utilization of these CP inhibitors outspreads to candidates for antiprotozoal action and to cysteine cathepsin inhibitors of interest in human diseases.

3.1.1. Structure activity relationships (SARs) and molecular dynamics simulations of known potent cruzain inhibitors as Cross-Class CP inhibitors

Matched molecular pair (MMP) analysis provides the opportunity to evaluate molecular modifications for significant structure–activity relationships (SAR). The analysis was performed in molecular pairs that differ only in positions where there is a promising chemical transformation. In this approach, transformations occur by identifying the change from one functional group to another in which its regiochemistry is also considered. MMP analysis can be useful to interpret bimolecular recognition process and the individual contributions of

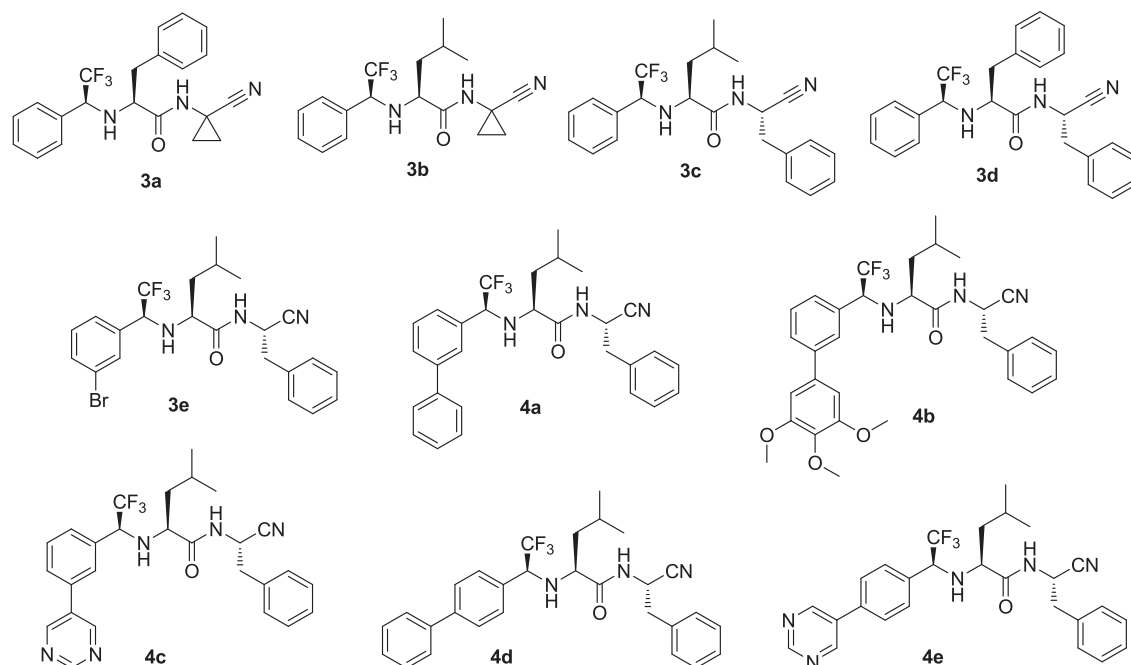


Fig. 2. 2D Structure representation of compounds 3a-3e and 4a-4e.

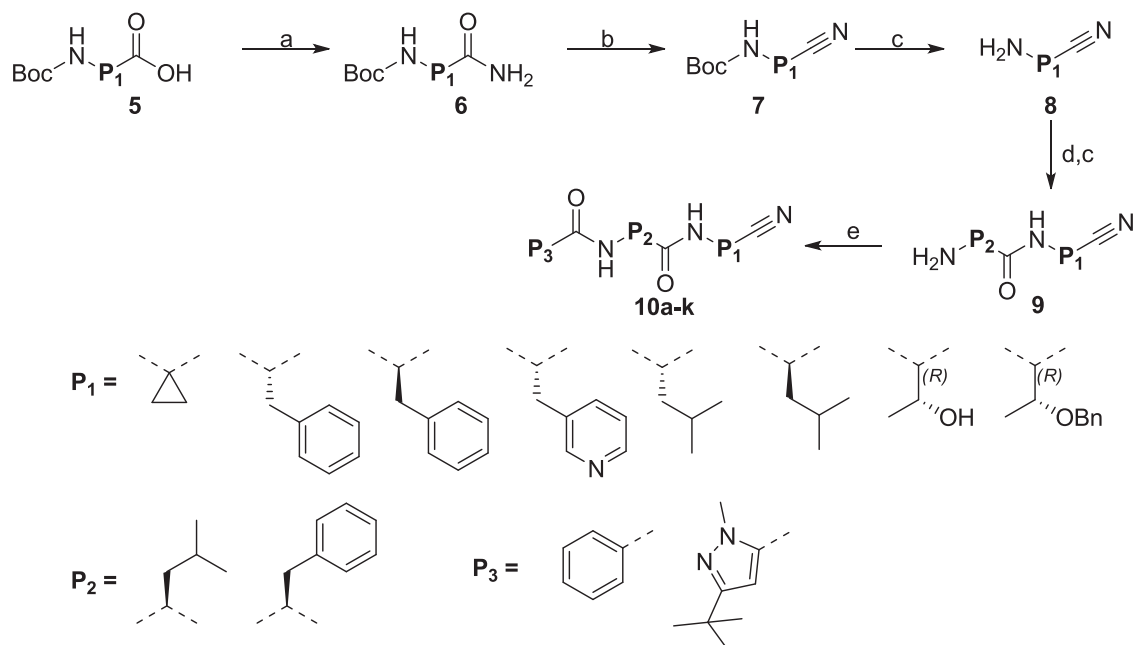
each transformation in that process [26].

The MMP/SAR analysis [26] considered the differences in affinity related to a structural transformation, defined as ΔpK_i . The ΔpK_i is calculated through the differences in affinity between two molecules (e.g., $\Delta pK_i = pK_i [10c] - pK_i [10d]$). ΔpK_i values inferior to 0.2 log units were considered not significant for affinity, and such transformation is genuinely characterized as a bioisosteric replacement. For selectivity, a ΔpK_i equal or higher than 1.0 log units was considered significant. As a starting point for the SAR analysis we have used compound 10c as a prototypical scaffold, which has high structural similarity with other dipeptidyl nitrile inhibitors co-crystallized with Cz and CatL [9,27]. Therefore, 8 compounds with different substituents at the P1, P2, and P3 positions and different stereochemistries were

evaluated as shown in Fig. 4.

Structural modification at the P3 position by altering 3-(tert-butyl)-1-methyl-1H-pyrazole (10c) to the phenyl group (10a) led to a loss of affinity for almost all CPs except CatS. The difference in affinity can be explained, for instance, by a van der Waals interaction between the methyl group of the 3-(tert-butyl)-1-methyl-1H-pyrazole and the Leu69 residue in the S3 pocket of CatL [27]. On the other hand, CatS contains a Phe70 residue in the S3 pocket which can perform π - π stacking interactions with the phenyl ring of the inhibitor without having enough space to accommodate the bulkier 3-tert-butyl-N-methyl-pyrazole group [28].

Modification in P2 by changing Phe (10c) to Leu (10d) led to an affinity gain for Cz and CatS with the highest affinity observed for CatK



Scheme 2. General synthesis of compounds 10a-10k. Reagents and conditions: a) Isobutyl chloroformate, DIPEA, DMF, argon, -30°C , 0.5 h, 2 M NH_4Cl , r.t., 20 h; b) DIPEA, THF dry, TFAA, $0^\circ\text{C} \rightarrow \text{r.t.}$, 2 h; c) HCO_2H , r.t., 5–18 h; d) *N*-boc-**P2**- CO_2H , HATU, DIPEA, DMF, r.t., 7–20 h; e) **P3**- CO_2H , HATU, DIPEA, DMF, r.t., 7–20 h.

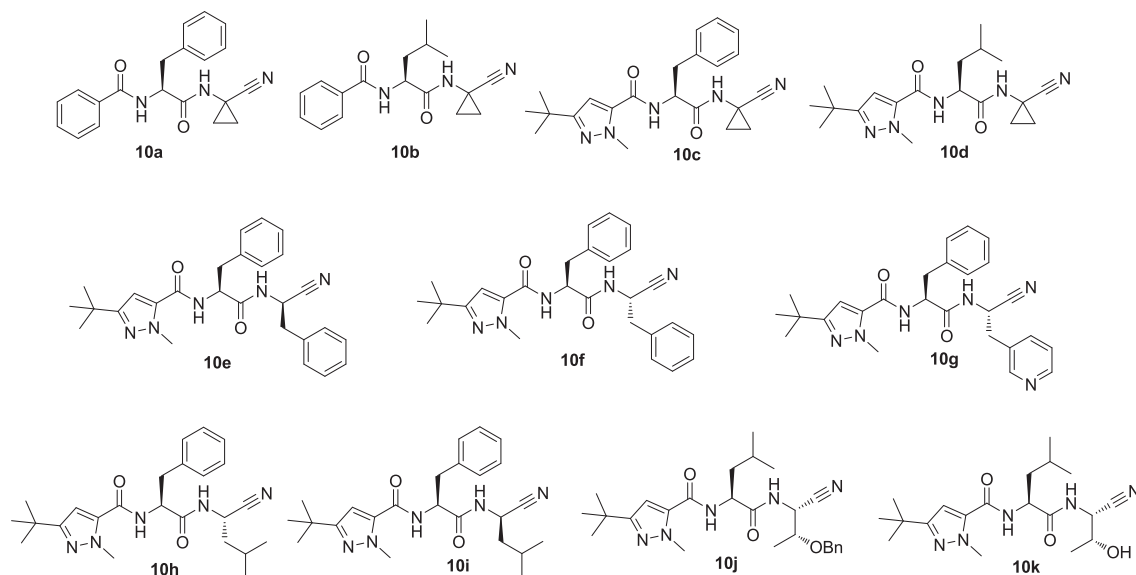


Fig. 3. 2D Structure representation of compounds 10a-10k.

Table 3

Enzyme inhibition. $pK_i = -\log_{10}(K_i/M)$. ^aThe standard deviation was lower than 15% for all reported pK_i values. pK_i values of compounds 10a-10k were reported recently [7]. N/D = Not determined.

Compound	pK_i values ^a				
	Cz	LmCPB	CatK	CatL	CatS
3a	6.1	5.8	5.4	6.8	7.2
3b	7.3	6.9	7.0	7.4	7.6
3c	8.7	8.6	8.6	8.8	8.7
3d	7.6	7.7	6.9	8.5	8.2
3e	8.8	8.3	8.7	9.4	8.4
4a	8.4	7.8	8.3	8.0	N/D
4b	8.3	7.3	7.3	6.9	7.9
4c	8.8	8.6	8.5	8.1	8.4
4d	9.2	9.1	N/D	5.8	N/D
4e	8.7	8.4	7.6	7.6	8.4
10a	6.7	6.6	6.4	7.4	7.3
10b	7.3	6.8	7.2	7.7	8.0
10c	7.3	7.1	6.5	8.2	6.8
10d	7.8	7.3	8.3	7.6	7.4
10e	6.3	6.1	5.6	6.9	5.9
10f	7.7	7.8	6.3	8.5	7.3
10g	7.5	7.2	6.5	8.3	7.2
10h	7.5	7.4	6.7	8.3	6.9
10i	6.5	6.4	6.0	7.0	6.0
10j	7.9	7.7	7.8	7.2	7.3
10k	7.1	6.7	7.8	7.0	5.0

(+1.8 log units). CatL was negatively affected as expected due to its preference for aromatic residues in the P2 position.

Relevant structural modifications in P1 are observed for five compounds. Not surprisingly, the (*S*) configuration of the moiety in P1 was preferred rather than the (*R*) configuration, as also observed in a recent study for amino acids substitution in P2 [29]. The substitution of the cyclopropane for aromatic moieties as the (*S*)-benzyl (10f) increased the affinity values for all CPs. The exchange of the cyclopropane for the isopropyl group (10h) did not lead to any improvement.

The substitution of the cyclopropane to the pyridine group (10g) maintains the affinity for all the CPs. Despite no significant change in affinity, pyridine raises the solubility of the inhibitor without modifying the main hydrophobic interaction with the target protein. This first MMP/SAR (Fig. 4) revealed that Leu in P2 and (*S*)-benzyl moiety in P1 are privileged structures for the design of new cross-class inhibitors amongst different CPs.

Other structural modifications at the P1 position were investigated among pairs of compounds, as shown in Fig. 5.

The modification in P1 from 10k to 10j led to a strong gain in affinity for Cz, LmCPB and CatS, while for CatL there was no meaningful difference in pK_i values. Noteworthy, an activity cliff [30] was observed for CatS when going from 10k to 10j. Transformation for the inclusion of the benzyloxy group in P1 resulted in a CatS affinity gain that exceeded 2 log units.

Recently, we have demonstrated that the description of covalent and noncovalent states of covalent inhibitors of CatL are important to describe the reversible covalent binding of dipeptidyl nitrile inhibitors [12]. In this work, we perform MD simulations for 10k and 10j inhibitors in complex with CatS. We have selected these two compounds for MD simulation, since they present the so-called activity cliff. Note that we have explored only the noncovalent state for both 10k-CatS and 10j-CatS complexes to investigate if P1 structural modification can influence the noncovalent binding mode of these ligands and consequently influence the covalent bond formation with Cys25 residue in the S1 pocket of CatS. Interestingly, after 60 ns of MD simulation the 10k left the active site of CatS, while 10j remain in the active site along 100 ns of MD simulation (Fig. 6). It is important to point out that the nitrile group of 10j is close to Cys25 residue, which suggests that the 10j is well positioned in the active site of CatS (see Fig. S2) and this ligand is more likely to form a covalent bond with Cys25 residue. On the other hand, the formation of the covalent complex is less likely to occur for the process involving CatS and 10k ligand. The binding process of covalent inhibitors consists of multiple steps. CatS and its inhibitor form a non-covalent complex, followed by the approach of the warhead to Cys25 and, finally, the formation of the covalent bond. We thereby can assume that the noncovalent state of 10k with CatS does not allow the formation of the covalent bond, yielding to a lower affinity (pK_i). Indeed, analyzing the pose of 10j at 15 ns (Fig. 6) the benzyloxy group is buried into a region of aromatic amino acids (e.g. Phe145, Trp186) and an arginine (Arg142) which can help to hold the compound in the active site (see Fig. S4). The free hydroxyl group (10k) is detrimental to the formation of the non-covalent complex, since it does not provide any help to keep the compound close to Cys25.

Also, noteworthy, the 3b → 3c transformation resulted in steep affinity gain for the five CPs. To investigate the effect of this transformation, we explored its matched molecular pair by the deconstruction of one-digit nanomolar pan inhibitor 3c to the moderate CP inhibitor 10a through a double SAR cycle (Fig. 7). The double SAR cycle reveals

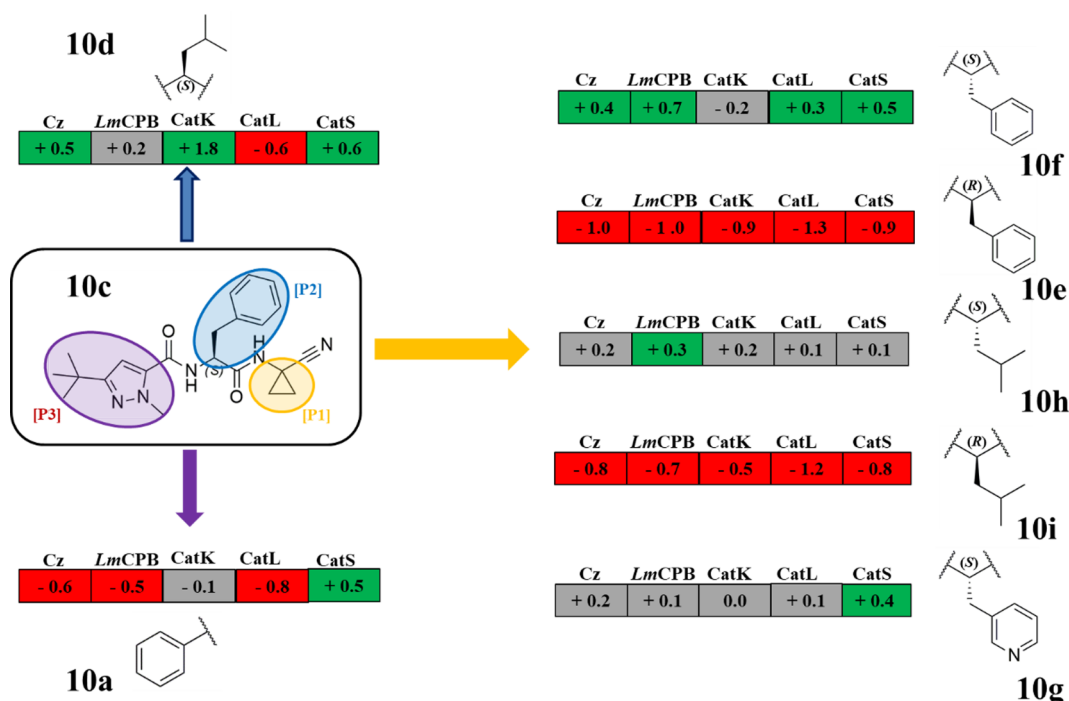


Fig. 4. MMPA/SAR summary for compound **10c**. Values are reported as differences in pK_i values and are color-coded as red (negative), green (positive), grey (no significant difference, $\Delta pK_i < 0.2$). Modifications in P1 are highlighted as orange, P2 blue and P3 purple. (For interpretation of the references to color in this figure legend, the reader is referred to the web version of this article.)

a non-additive effect on SAR, which is particularly valuable for testing and validating different interaction modes [31]. The values of inhibition constants are shown on the left side of compound **10a** and on the right side of **3c** for all studied CPs. Table 4 presents all pK_i value differences for the respective transformations shown in Fig. 7.

The upper part of the cycle consists of a *semi-flat* SAR because there are no significant gains in affinity. At the same time, all transformations observed in this part of the cycle are superadditive. The structural transformation related to the ΔpK_i of [**10a** → **10b**] were below 1.0 log units. The individual transformation of [**10a** → **3a**] diminished the affinities of the five CPs. These losses are mainly observed for Cz, LmCPB, CatK and CatL, but not for CatS whose decrease was only 0.1 log unit. This result suggests that the bioisosteric replacement of the C=O bond to the CF₃ group is better tolerated in CatS. On the other

hand, the transformation [**10b** → **3b**] produced a less negative effect for most of the CPs. The substitution of the Phe for Leu in P2 [**3a** → **3b**], while maintaining the CF₃ group, produced an increase in affinity of almost 100 times. Therefore, the combination of the CF₃ group with the Leu at the P2 position has a superadditive effect on affinity for all the CPs.

For the lower part of the cycle, which leads to **3c** from **3a**, the structural transformations for the five CPs were all additive as the differences in ΔpK_i were between $\pm 0.1/0.2$ log units, all having been considered real bioisosteric exchanges without increased affinity. A massive improvement in affinity was obtained when observing the lower part of the cycle. One could justify these phenomena by considering that when the CF₃ is implemented, the mode of binding (MoB) of the inhibitors change, allowing a better accommodation of P1, P2

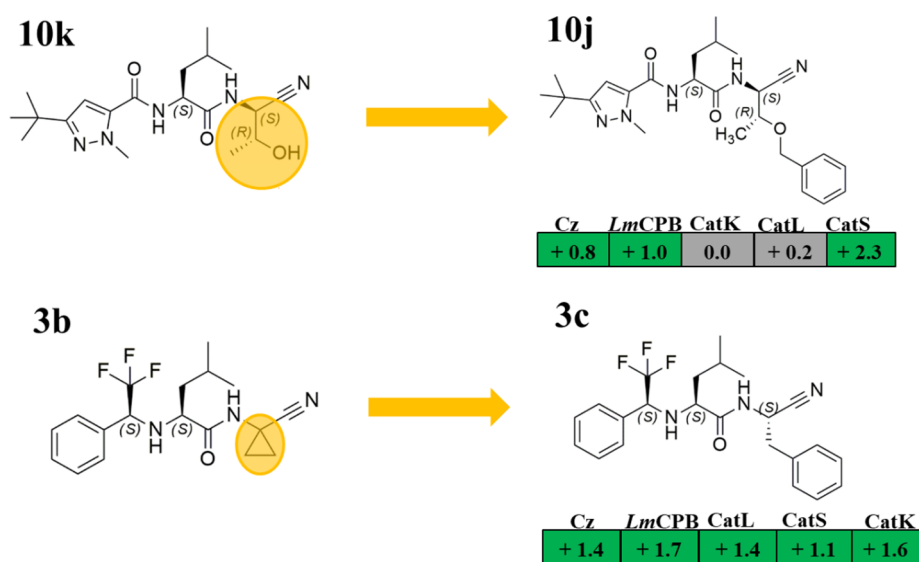


Fig. 5. MMPA/SAR summary for compounds **10k** and **3b**. Values are reported as differences in pK_i and are color-coded as green (positive) and grey (no significant difference, $\Delta pK_i < 0.2$). Modifications in P1 are highlighted as orange. (For interpretation of the references to color in this figure legend, the reader is referred to the web version of this article.)

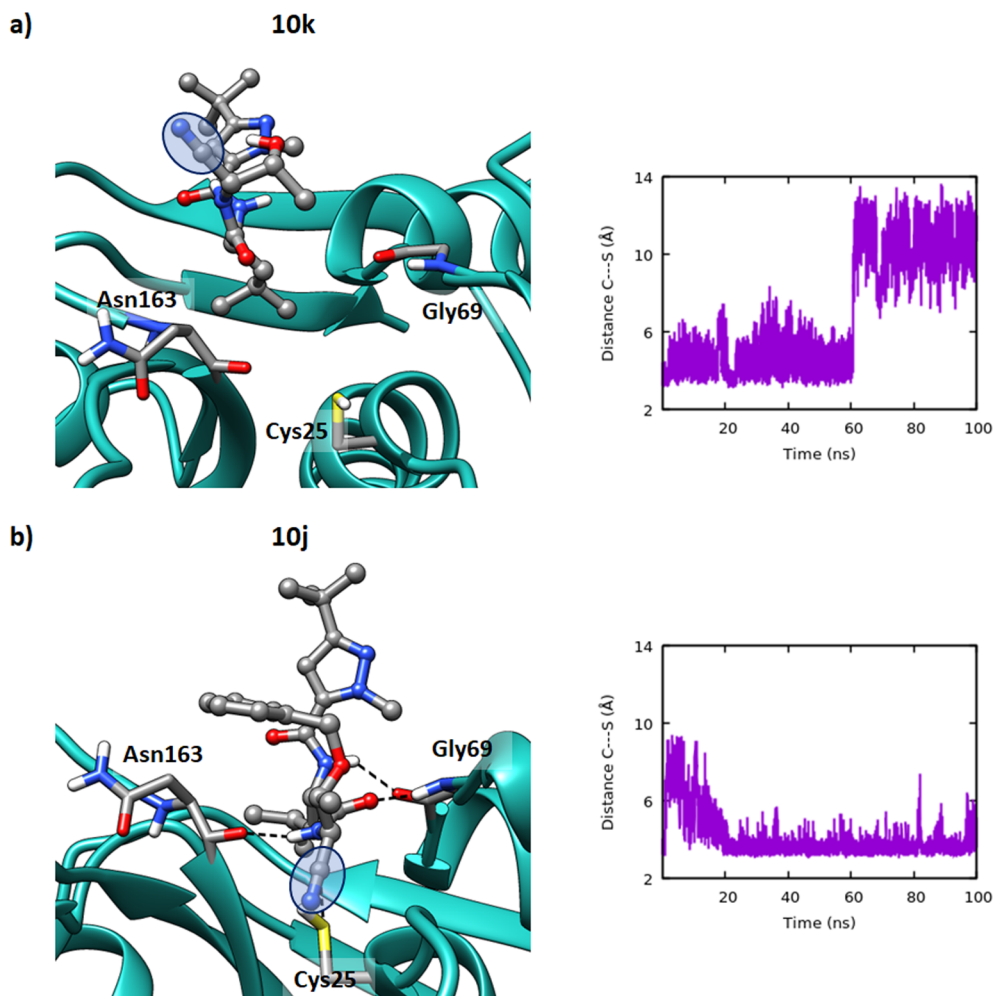


Fig. 6. Mode of binding of compounds **10j** and **10k**. Snapshot was taken at 95 ns of a 100 ns (non-covalent MD simulation). Hydrogen bonds, when occur with Asp163 and Gly69, are represented in dashed lines. Warhead is highlighted as blue. The distance (Å) fluctuations between nitrile carbon with sulfur of Cys25 were also represented on the right side. The backbone of CatS is light green. The main residues and carbon chains are greys, nitrogen is blue, oxygen is red, sulfur is yellow. a) **10k**-CatS non-covalent complex. b) **10j**-CatS non-covalent complex, the interaction of the nitrile carbon with sulfur from Cys25 is also represented. (For interpretation of the references to color in this figure legend, the reader is referred to the web version of this article.)

and P3 moieties in the subsite pockets leading to the strong cross-class inhibitor (**3c**) with a K_i of about 3 nM for all the five CPs. Nonetheless, it is worth mentioning that the chemical transformations implemented in the dipeptidyl nitrile scaffold **10a** that resulted in the elaboration of the non-peptide inhibitor **3c**, had an average affinity gain of more than 60 times in all studied CPs. The most striking affinity gain of over 100 times is not only observed for Cz and LmCPB (the two parasitic targets), but also for CatK. It is also important to mention that the transformation **3a** → **3c** resulted in a gain of 2.6 log units leading **3c** to a synergistic gain of about 400 times over **3a** after only a small cycle of molecular modifications.

3.1.2. Structure activity relationships (SARs) and molecular dynamics simulations of new Non-Peptidic nitrile based Cross-Class CP inhibitors

Recently, we have outlined that the *para*-biphenyl moiety that is in the P3 position of a trifluoroamine derivative is a privileged structure for leveraging Cz affinity while gaining selectivity over CatL [8]. However, due to the undesirable physicochemical properties of the compound, such as low water solubility and high lipophilicity, we modified the aryl ring by a pyrimidine to introduce **4e** (Fig. 8). To improve its water solubility while maintaining affinity for Cz, **4e** is still significantly selective (1.1 log units) over CatL. Compound **4e** was thereby re-engineered to include the 5-phenylpyrimidine moiety giving **4c** (Fig. 8). The synthesis was performed by following the same procedure for compound **4e** [8]. None of the implemented modifications led to a considerable increase in affinity for protozoan CPs. On the other hand, the *meta*-bromine (**3e**) in P3 produced a strong increment in affinity for both CatL and CatK. The affinity cliff for CatL inhibition

observed for the pair [**4e** → **3e**] can be addressed by an halogen bond interaction with the Gly61 [12]. It is noteworthy that while *para* 5-phenylpyrimidine in P3 is a privileged moiety for maintaining affinity between protozoa and mammalian CPs, *meta*-substitution appears to play a particular role amid cross-class inhibitors of different CPs, such as **3e** and **4c**. It is also striking that all CPs lost affinity for compound **4b** that bears the 3,4,5-trimethoxy-1,1'-biphenyl moiety.

Molecular dynamics simulations were performed to better investigate the putative mode of binding of **4a**, **4c**, **4d** and **4e** derivatives when bound to Cz. It is known from experimental data that dipeptidyl nitrile-like molecules form hydrogen bonds to the backbone NH and C=O groups of Gly66 and Asp161 in the Cz active site [9]. The mean distances of these key interactions computed during 100 ns of MD for **4d** in complex with Cz are depicted in Fig. 9, for the other ligands these mean distances are shown in SI.

The average distances obtained in the MD simulations show that Gly66 is positioned to form two hydrogen bonds with the hydrogen of the trifluoroethylamine group and the oxygen of the amide bond. Too, Asp161 interacts with the ligands through hydrogen bonding with the hydrogen of the amide bond in P2/P1 position. Gly66 and Asp161 residues form hydrogen bonds to all ligands in the covalent complex and maintain their stability during 100 ns of the molecular dynamics. This result shows that ligands maintain the same key interactions at the active site of Cz.

Fascinatingly, visual inspection of molecular dynamics simulations brings up two putative modes of binding (MoB) for all four compounds. In the first MoB I (see Fig. 10 compound **4c**), P3 is in contact with the S3 surface and CF₃ is exposed to the solvent. While in the MoB II (see

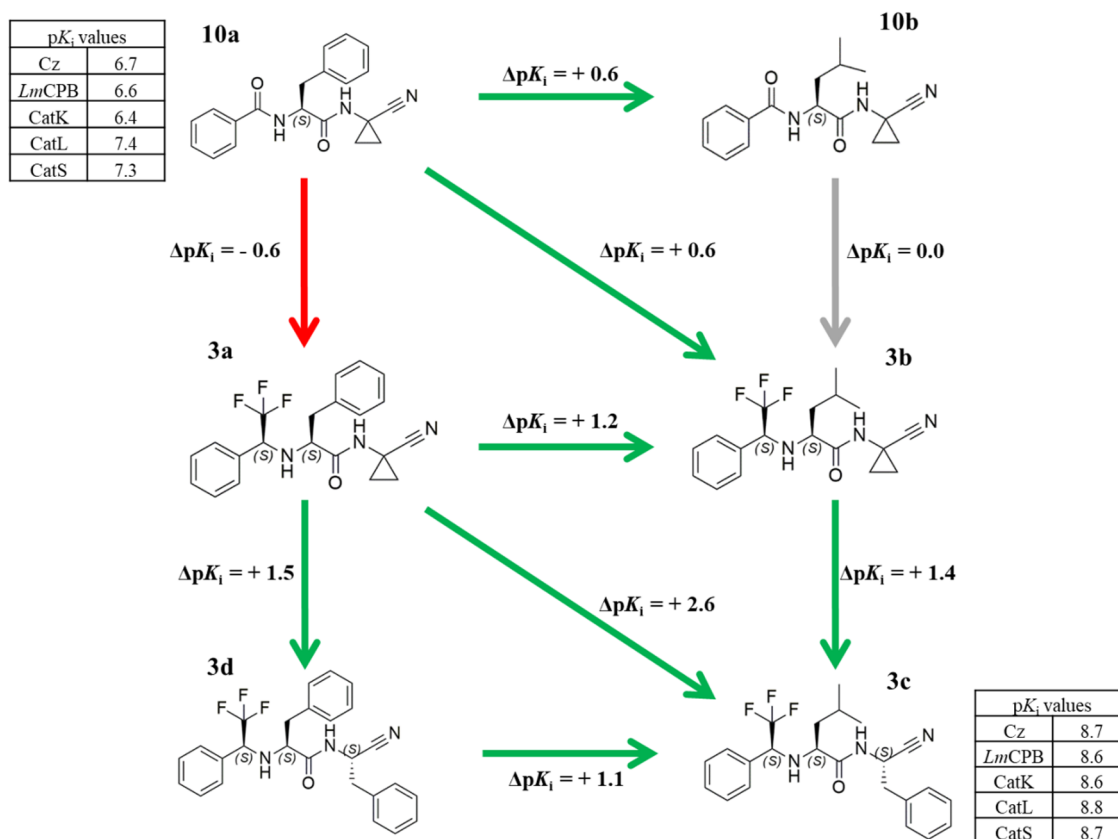


Fig. 7. Double cooperativity cycle for transformations of compounds **10a** to **3c** for cruzain inhibition. Values are reported as differences in pK_i for Cz inhibition. Green arrows highlight positive trend while the red arrow depicts a negative trend. (For interpretation of the references to color in this figure legend, the reader is referred to the web version of this article.)

Table 4

ΔpK_i from the SAR analysis of Fig. 7. The notation [X → Y] indicates a structural modification. Diagonal transformations are highlighted in orange.

Structural modification [X → Y]	Cz	LmCPB	CatK	CatL	CatS
[10a → 10b]	+ 0.6	+0.2	+0.8	+0.3	+0.7
[10a → 3a]	-0.6	-0.8	-1.0	-0.6	-0.1
[10a → 3b]	+0.6	+0.3	0.0	0.0	+0.3
[10b → 3b]	0.0	+0.1	-0.8	-0.3	-0.4
[3a → 3b]	+1.2	+1.1	+1.6	+0.6	+0.4
[3a → 3d]	+1.5	+1.9	+1.5	+1.7	+1.0
[3a → 3c]	+2.6	+2.8	+3.2	+2.0	+1.5
[3b → 3c]	+1.4	+1.7	+2.2	+1.4	+1.1
[3d → 3c]	+1.1	+0.9	+1.7	+0.2	+0.5

Fig. 10 compounds **4a**, **4d** and **4e**), the CF₃ group is straight towards S3, while the P3 group is forming an intramolecular π stacking interaction between hydrogen in position 2 of the aryl ring at P3 and the phenyl group at P1 (**Fig. 10**).

In general, the starting point of the simulation displays the MoB I for all four compounds. However, compounds **4a**, **4d**, **4e**, switch to MoB II in < 40 ns and maintain this conformation for the rest of the simulation, while compound **4c** maintains the MoB I for 90% of the simulation (**Fig. 11**). Hence, the main configuration responsible for the binding process interaction is MoB II for compounds **4a**, **4d**, **4e**; while for compound **4c** the main bimolecular interaction arisen by the MoB I. This difference can be arisen by the possibility of compound **4c**, which bears a pyrimidine ring in *meta* position, to interact with Ser61 by hydrogen bonding when forming the MoB I but not when performing the MoB II. Indeed, **4e** which bears a pyrimidine ring in P3 but in *para* position show not substantial interaction with the Ser61 over the

simulation and therefore the MoB II with the formation of an intra-molecular interaction is favorable (**Fig. S5**). Compound **4a**, which bears a *meta* biphenyl ring in P3 display a strong preference for the MoB II for over 90% of the simulation where the biphenyl ring is fully solvent-exposed while the hydrogen in position 2 of the aryl ring is pointing towards the center of the phenyl ring in P1 with an angle of about 90°. Similar behavior is displayed by compound **4d**, which has a weak interaction with the Ser61 when performing the MoB I, and therefore it switched to MoB II after 30 ns forming intra-molecular interactions for the rest of the simulation.

Since the difference in pK_i values amid these four compounds is very small, it can be assumed that both putative MoBs contribute positively to Cz affinity and are in equilibrium with each other. However, we have recently published a strong non-additivity SAR for Cz inhibition [8] which can be explained by the presence of MoB I and MoB II. Indeed, if we consider **Neq0658**, as molecular pair of compound **4d**, which can just adopt the MoB I (**Fig. S12**), due to its different configuration of the carbon in P3 we experienced a drop of almost three log unit in affinity with a strong nonadditivity relationship in affinity (**Fig. 12**) [8]. Hence, new in-depth studies should be carried out to better estimate the existence and influence of the MoB II over the general bimolecular recognition process.

3.2. Thermodynamic cycle and ITC evaluation

As already described in our recent study [32], isothermal titration calorimetry (ITC) is a technique used for the thermodynamic characterization of interactions amongst biomolecules and small molecules, which is vital for understanding the process of molecular recognition. Therefore, we have performed an in-depth analysis of the thermodynamic profiles for the key compounds with Cz to better estimate how

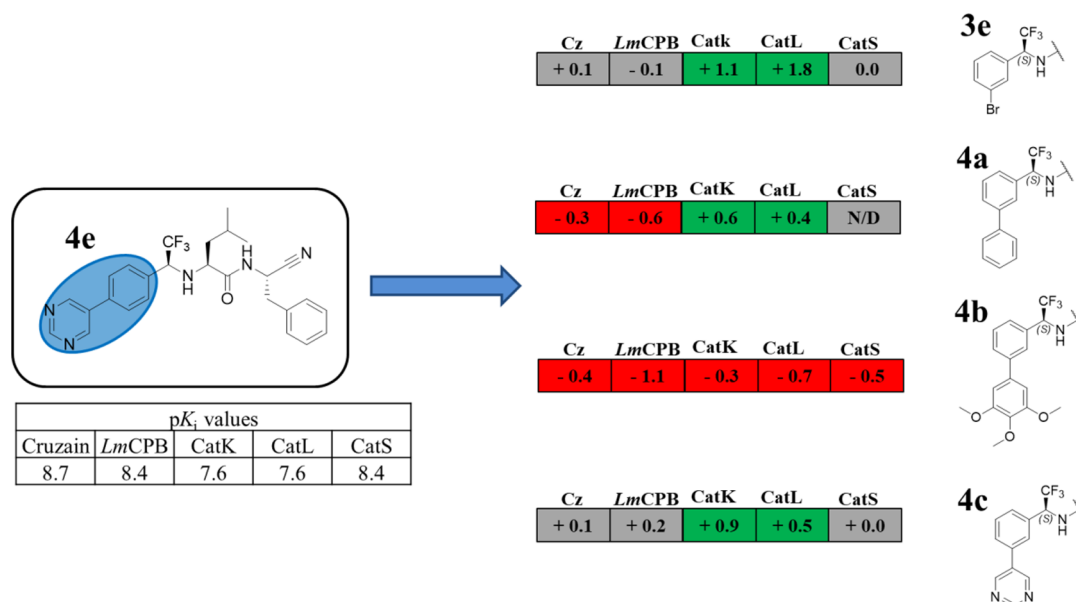


Fig. 8. MMPA/SAR summary for compound **4e**. Values are reported as differences in pK_i and are color-coded as red (negative), green (positive), grey (no significant difference, $\Delta pK_i < 0.2$). (For interpretation of the references to color in this figure legend, the reader is referred to the web version of this article.)

small chemical modification affected the SAR (Table 5) when the binding energy is dissected in its enthalpic and entropic terms.

The binding energy ΔG is the result of enthalpy (ΔH) and entropy (ΔS) contributions. Classically, enthalpy reflects the strength of the interactions due to the formation of hydrogen bonds and van der Waals interaction, while the binding entropy is a combination of the change in the desolvation and conformational changes after the formation of the bimolecular ligand-cruzain complex [33].

As can be seen from Table 5, there is a slight variation in the binding energy values (ΔG) and all of them round to median of -9.8 ($se = 0.2$ and $sd = 0.7$). Thus, although all interactions are favorable for Cz-inhibitor complex formation, optimization of ligands through binding affinity may not be trivial. Since ΔG binding affinity is determined by changes in enthalpy and entropy, it is desirable to establish any existing correlations between enthalpy and entropy to evaluate any compensation (EEC) as well as the correlations arising from the enthalpy/

entropy-structure activity relationships. Fig. 13a shows that ΔG is mirrored by both enthalpy and entropy, which is reflected by the linearity between enthalpy and entropy (Fig. 13b): $R^2 = 0.928$, $R^2_{adj} = 0.921$, with clear homoscedasticity seen in Fig. 13c residuals.

Beyond this classical interpretation of EEC, we can observe in the analysis of the thermodynamic signatures (see Fig. 14a below) that most of the compounds have, as depicted, a detrimental entropy contribution. Nonetheless, both enthalpy and entropy play a favorable role for the binding energy of compounds **10g** and **4e** (red bars), while displaying an opposite compensation effect which yields to the lowest values of enthalpy contribution [34].

The affinity K_a , which is governed by the Gibbs binding energy (ΔG : $K_a = e^{-\Delta G/RT}$), summed up by enthalpy and entropy ($\Delta G = \Delta H - T\Delta S$), does not necessarily result in high affinity when their favorable contributions are observable (see Fig. 14a). Although we would much prefer simultaneous optimization of enthalpy and entropy, it is clear

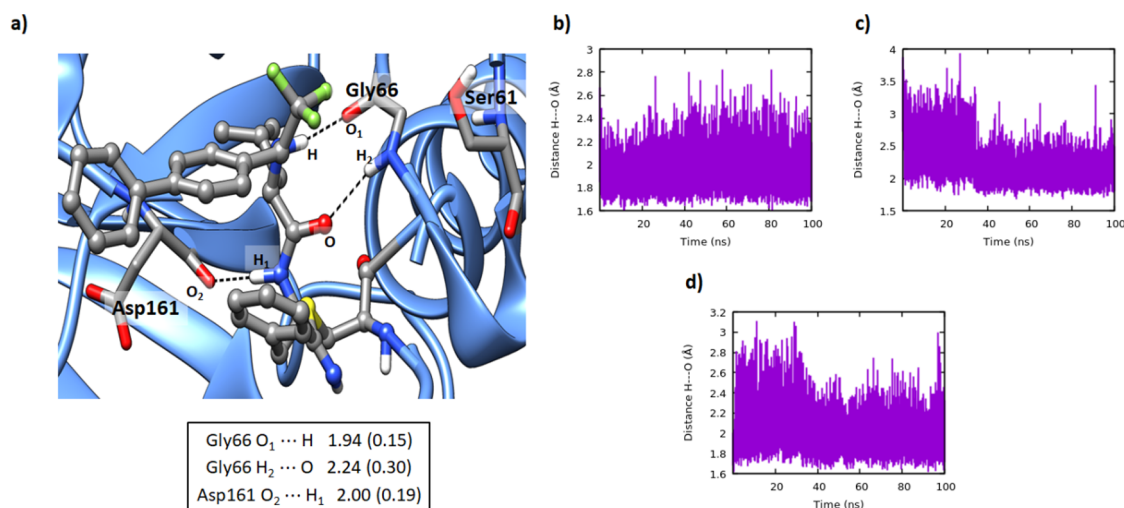


Fig. 9. Covalent molecular dynamics simulation for **4d**-Cz complex and key interactions. a) Snapshot was taken at 85 ns of a 100 ns simulation for **4d**-Cz complex and key interactions in Cz active site. b) Hydrogen bond (Hb) distance (Å) fluctuations between O₁ of Gly66 and H of the ligand. c) Hb (Å) fluctuation for H₂—O distance. d) Hb (Å) fluctuation between O₂ of Asp161 and H₁ of the ligand. Average values are shown in the box, along with the standard deviation in parenthesis. The backbone of Cz is blue. The main residues and carbon chain of **4d** are grey, fluorine is green, nitrogen is blue, oxygen is red, sulfur is yellow. Hydrogen bonds are depicted by dashed lines. (For interpretation of the references to color in this figure legend, the reader is referred to the web version of this article.)

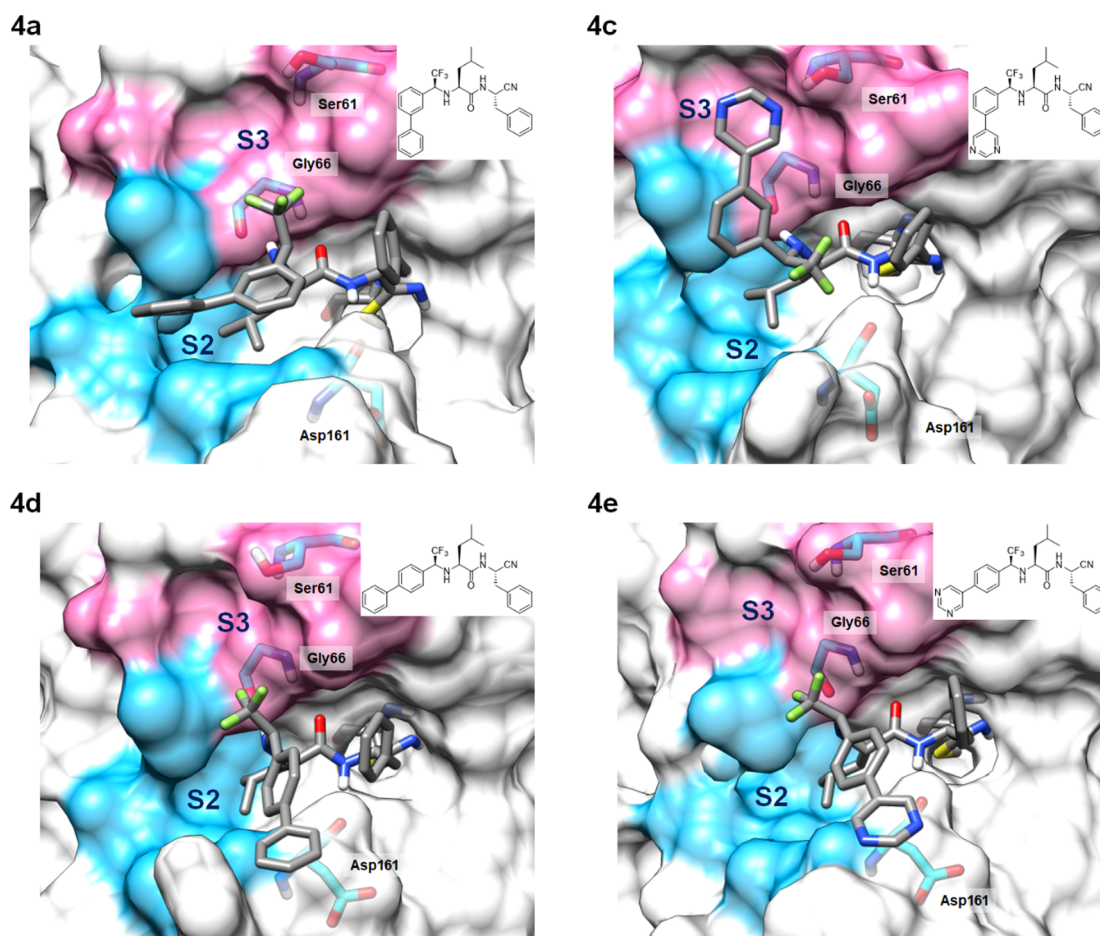


Fig. 10. Major putative mode of binding of compounds **4a**, **4c**, **4d**, **4e** with Cx. Compound **4c** displays a major MoB I. Compounds **4d**, **4e** and **4a** show a preference for MoB II. Cx surface is depicted in grey. S2 pocket is light blue. S3 pocket is pink. The main residues and carbon chain of ligands are grey, fluorine is green, nitrogen is blue, oxygen is red, sulfur is yellow. (For interpretation of the references to color in this figure legend, the reader is referred to the web version of this article.)

from Fig. 14a that the present process is enthalpy-driven (blue bars). The enthalpy contribution (median of -12.8 , $se = 0.7$, $sd = 2.6$, variance = 6.9, blue bars) is stronger than the entropy (median of 3.2, $se = 0.7$, $sd = 2.6$, variance = 7.1, dark blue bars) within this series of Cx inhibitors. Overall, the Gibbs binding energy remains almost the same at the median of -9.9 , $se = 0.2$, $sd = 0.7$, variance = 0.5 – light blue bars.

The binding entropy on the other hand, being dependent primarily on the hydrophobic effect seems to characterize the pattern observed for cruzain inhibitors herein under study via ITC. Fig. 14(b, c, d) shows the comparative profiles amongst compounds that present favorable and unfavorable entropy for inhibitors that are the main directors of bimolecular interaction. These Boxplots depict qualitatively a trend that the two inhibitors with favorable entropy (**Fe**, cyan Boxplots) for the composition of Gibbs binding energy, have higher lipophilicity, molecular mass, and topological polar surface area than those observed for inhibitors with detrimental entropy (**De**, green Boxplots).

It is striking that the binding thermodynamics can discriminate between inhibitors with good and bad entropy contributions. The binding affinity observed also depends on the size of the ligands (Fig. 14c) and this observation appears to be in line with medicinal chemistry practice of adding new functional groups to improve affinity [35]. To the same extent, Gibbs binding energy is leveraged to its median via lower enthalpy with higher entropy gain for inhibitors **10g** and **4e** – as compared to the other inhibitors that present detrimental entropy. Too, high lipophilicity and the highly polar character expressed by the large polar surface area of **10g** and **4e** amalgam favorably towards the desired thermodynamic profile of these Cx inhibitors

(Fig. 14a, light and dark blue and red bars favorable profile scheme – the enthalpic and entropic parameters contribute positively to the binding energy). Although the correlation may seem contradictory, there is a tendency for an inverse correlation between lipophilicity and topological polar surface area (TPSA). For instance, in a series of 443 cruzain inhibitors retrieved from the ChEMBL database [36], there is a poor correlation between SlogP and TPSA whose R^2 is only -0.153 . For the case of a small but significant series studied here, this trend appears also to be valid since the value of R^2 is -0.376 .

The graph in Fig. 13b above shows the classic representation of the correlation between $-T\Delta S$ and ΔH . It is observed a clear linear dependence that encompasses both the detrimental and favorable entropy contributions (both processes being spontaneous at the studied temperature), while the values of ΔG remains balanced throughout the series (Table 5). Thus, we wanted to better evaluate such relationships and the results are shown in Fig. 15.

Fig. 15a represents the observed changes in entropy (favorable-unfavorable) for bimolecular interactions that are enthalpy-driven (favorable enthalpic contribution) in relation to Gibbs binding energy. The bimolecular recognition pattern so depicted, aligns compounds **10g** and **4e** within the space comprised by favorable entropy inhibitors, with the “similar” ΔG value centered at $-9.5 \text{ kcal mol}^{-1}$. This equivalence in binding energy escapes EEC, but the nature of the factors that affect it remains uncertain. The result observed in Fig. 15b suggests that the ratio $(\Delta H + T\Delta S)/\Delta G$ might be a measure of the enthalpic driving force. The equal contribution of enthalpy and entropy to binding energy must be zero and positive when the binding is enthalpy-driving. Overall, the calculated ratio for the study compounds is positive but

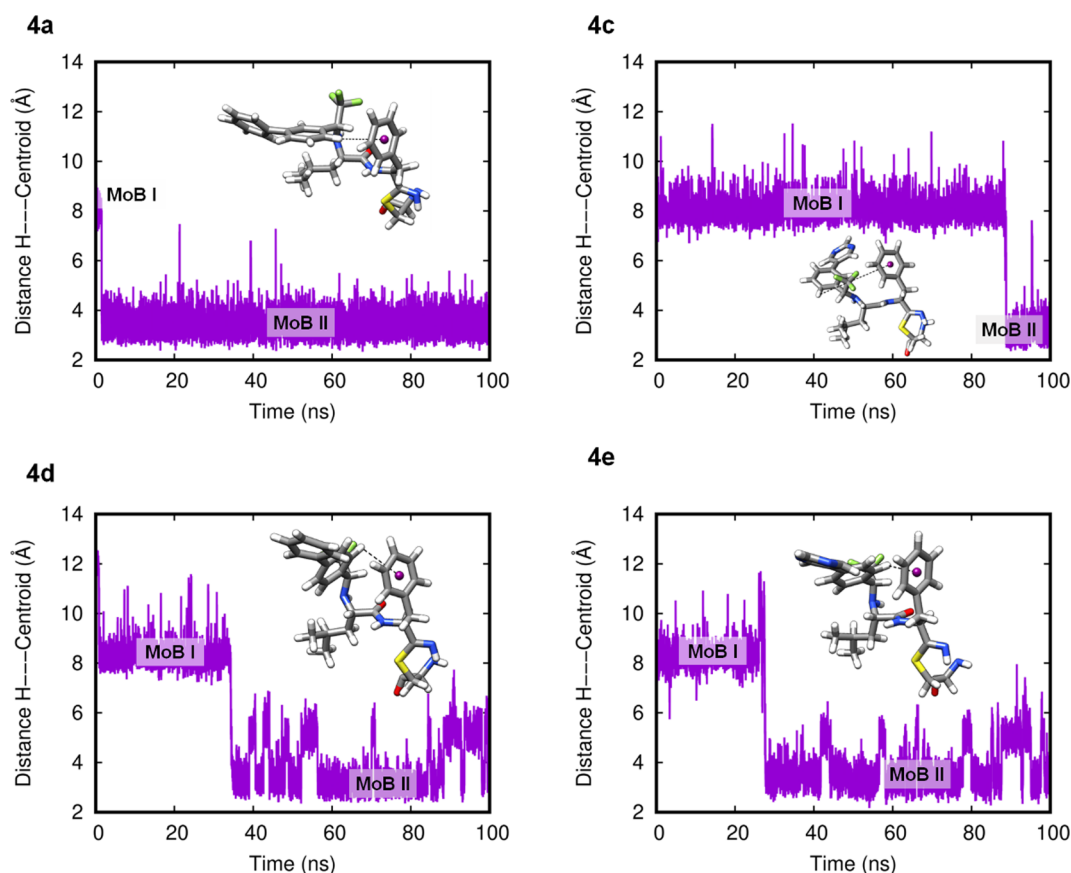


Fig. 11. Distance (Å) fluctuations between hydrogen located in P3 ring and the centroid of the benzene ring in P1. Interaction is represented inside the graphics. **4d 4e 4c 4a.** Carbon chain is grey, fluorine is green, nitrogen is blue, oxygen is red, sulfur is yellow. (For interpretation of the references to color in this figure legend, the reader is referred to the web version of this article.)

tends to zero for inhibitors **10g** and **4e**. For the other inhibitors, the values are greater than 1 and, thus, enthalpy overcompensates the unfavorable entropic contribution (Fig. 15b). The dimensionless ratio $(\Delta H + T\Delta S)/\Delta G$ dubbed the Enthalpy–Entropy Index (I_{E-E}) is, therefore, used to indicate the enthalpy content of the binding interaction. And, this may shed light directly towards thermodynamically-driven optimization endeavor. For instance, the inhibitors **3a**, **10a** and **10h** whose I_{E-E} is greater than 2 (2.57, 2.24 and 2.02, respectively) do not seem to surpass inhibitors **10g** and **4e** with I_{E-E} values of 0.705 and 0.499 in terms of their binding energies (ΔG) thereby confirming the trend that enthalpy optimization is not a trivial process [37].

The pharmacodynamic characterization of new drug candidates presupposes the determination of target-binding kinetics. Since the same set of ligands is used for fluorimetric assays (K_i) and ITC (K_d), it is reasonable to assume that there exists a correlation between the pK_i and pK_d values. Nonetheless, it is important to note that there are significant biochemical differences between K_d and K_i . Although related to each

other, K_i is dependent on the K_M value but K_d is not. K_d measures the balance between the target–ligand complex and its dissociated components, the reason for which it is given by the rate of constant dissociation for the complex and the association rate constant (k_{-1}/k_1). K_i , on the other hand, measures the reduction in the enzyme catalytic activity and, therefore, is dependent on the kinetic mechanism of inhibition, which, in the present case, is a competitive mechanism.

To initiate the correlation analysis between pK_i and pK_d we have built the plot of the kernel density estimate and histogram for both their values (pK_i in blue and pK_d in pink). As can be seen from Fig. 16a, there is an overlapping density in both data. However, because heteroscedasticity is present, it reduces the precision of the estimates in OLS linear regression. Also, the means are 7.02 and 7.30, with standard deviations of 0.512 and 0.817, respectively, for pK_d and pK_i values. So, we cannot employ ordinary least squares (OLS) to fit such data [38]. The scatter plot is shown in Fig. 16b. In order to circumvent this matter, we have employed a recursive least squares (RLS) method, which is an

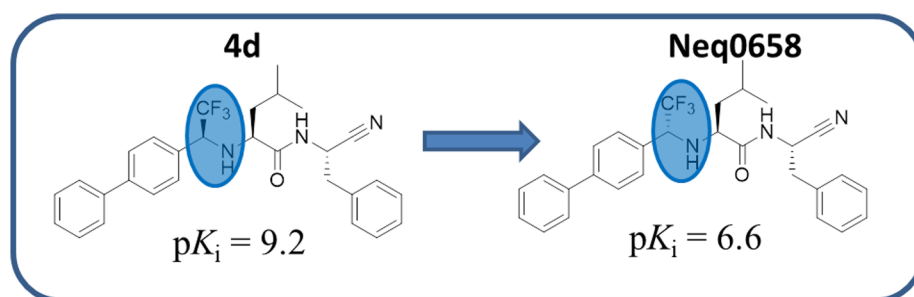


Fig. 12. MMFA for compound **4d**. Values are reported as pK_i for Cz inhibition.[8] Colored areas highlight the stereochemical modifications.

Table 5

Thermodynamic parameters of Cz-ligand complexes obtained from ITC experiments. $pK_d = -\log_{10}(K_d)$. Uncertainties are shown in parentheses. **In blue are highlighted 4e and 10g** for presenting favorable entropy to Gibbs binding energy.

N°	pK_d	ΔG (kcal mol ⁻¹)	ΔH (kcal mol ⁻¹)	$-T\Delta S$ (kcal mol ⁻¹)
3a	6.1 (0.07)	-8.3 (0.02)	-14.9 (0.1)	6.6 (0.1)
3b	7.3 (0.2)	-10.0 (0.2)	-13.3 (0.3)	3.2 (0.1)
4c	7.5 (0.02)	-10.3 (0.0)	-13.5 (0.5)	3.2 (0.5)
4e	7.1 (0.03)	-9.7 (0.04)	-7.3 (1.5)	-2.4 (1.5)
10a	6.6 (0.01)	-9.0 (0.02)	-14.6 (0.3)	5.6 (0.3)
10b	7.5 (0.03)	-10.2 (0.07)	-14.5 (0.7)	4.3 (0.7)
10c	7.2 (1.2)	-9.8 (0.5)	-12.2 (1.2)	2.4 (0.04)
10d	7.6 (0.08)	-10.4 (0.1)	-15.7 (0.08)	5.3 (0.9)
10e	6.2 (0.07)	-8.5 (0.07)	-11.9 (0.4)	3.4 (0.04)
10g	7.0 (0.1)	-9.5 (0.2)	-8.10 (0.5)	-1.4 (0.7)
10h	7.5 (0.1)	-10.2 (0.2)	-10.7 (0.6)	0.5 (0.4)
10i	6.5 (0.1)	-8.8 (0.02)	-11.6 (1.1)	2.8 (1.2)
10k	7.2 (0.09)	-9.9 (0.1)	-10.8 (0.5)	0.97 (0.6)

expanding window version of OLS [39]. The RLS statspace regression model results for fitting data from Fig. 16b is: $R^2 = 0.995$ for a pK_d slope of $1.04 (\pm 0.0220)$ with $z = 48.4$ and $P > |z| = 0$. The robust linear model (RLM) [40] yields a similar result ($P > |z| = 0$ for $z = 111$). The RLS model allows the calculation of the recursive residues with the statistics called the cumulative sum control chart (CUSUM) [41]. The plotting of these statistics, Fig. 16c, indicates that the CUSUM statistic (the blue line) does not expand outside the 5% significance limit.

3.2.1. Analysis of enthalpic and entropic contribution by thermodynamic cycles

The double transformation **10a** → **3b** (Fig. 7 above) occurs via an exchange of a carbonyl for a trifluoromethyl and phenylalanine group for leucine with a gain of only 0.6 log units in Cz affinity. However, this result *per se* does not bring qualified information about the real nature of the transformation in terms of the individual contributions of each modified group. An elegant way to evaluate the thermodynamic contributions to the molecular changes implemented on time is through the analysis of the change in enthalpy and entropy caused by such changes. As a matter of ease comparison, the relative differences ($\Delta\Delta X_{n \rightarrow m}$, $X = G, H$, and S) of the thermodynamic properties for a given transformation are shown in Fig. 17. These differences make it possible to analyze the distributions of the respective thermodynamic values for the pairs of inhibitors in such a way that the enthalpy effects and entropy are analyzed differently from the above sources of correlation. In addition, the sudden changes brought about by the transformations offer the opportunity to better assess the disturbance imprinted on the binding energy via individual group contribution.

In the specific case, from **10a** to **3b** two molecular changes were implemented. Thus, the analysis of enthalpic and entropic contributions is performed through a thermodynamic cycle (Fig. 17). The two ligands interact with similar binding affinity with similarly putative modes of interaction. Despite this, the Gibbs binding energy partition occurs differently as seen in the thermodynamic cycle in Fig. 17.

Thermodynamic cycle analysis for the double transformation from **10a** to **3b** reveals a superadditive effect in the free energy which is driven mostly by the entropy change contribution (Fig. 17). The single modification in P2 from Phe to Leu (**10a** → **10b**) leads to an indistinguishable difference in enthalpy change and a positive effect in the entropy change which can be rationalized by an increase of rotational bond in the molecule. On the other hand, the bioisosteric replacement of the carbonyl group for the CF₃ (**10a** → **3a**) precludes any gain. Transformation **3a** → **3b** results in a gain cliff in the change of entropy with a large loss in the enthalpic change. Cooperativeness is not seen in the transformation **10a** → **3b** despite the detrimental contribution of

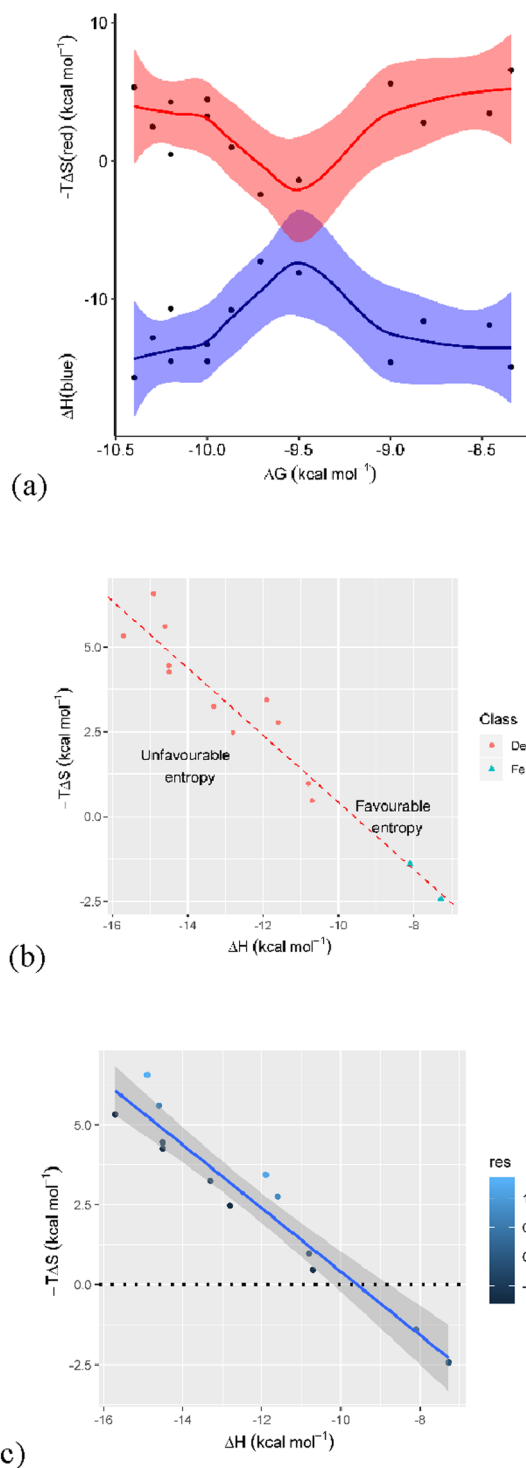


Fig. 13. Enthalpy-entropy compensation (EEC) observed for Cz-inhibitor complexes. (a) ΔG is mirrored by ΔH and $-T\Delta S$; (b) linear ($R^2 = 0.928$, $R_{adj}^2 = 0.921$) compensation between enthalpy and entropy: the most favorable enthalpy interaction imposes some restriction on the movement of interacting partners that results in an unfavorable entropic change. In line with it, the two Cz inhibitors **10g** and **4e** with favorable entropy help to contribute to the overall unchanged value of ΔG . In the box-legend to the right, De is for detrimental entropy whereas Fe stands for favorable entropy; (c) linear fit of $-T\Delta S$ vs ΔH as in (b) but along with the residuals (the right box-legend of black to blue), which represents the homoscedasticity of the residual entropy. (For interpretation of the references to color in this figure legend, the reader is referred to the web version of this article.)

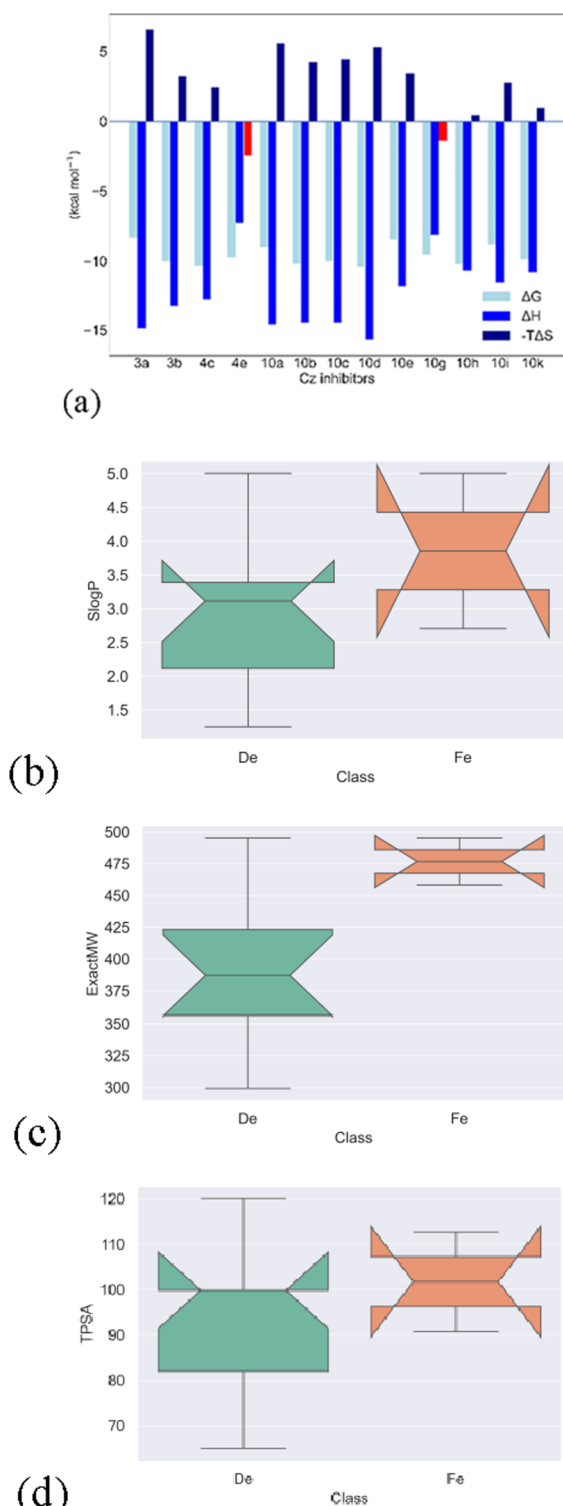


Fig. 14. (a) Thermodynamic signature to access the magnitude of the thermodynamic forces that contribute to the binding energy (ΔG), binding enthalpy (ΔH) and binding entropy ($-T\Delta S$). The profile is typically enthalpy-driven but the enthalpy-entropy balance for cruzain inhibitors is dominated by detrimental contribution from entropy with the exception of **4e** and **10g** that modulate bimolecular recognition via favorable enthalpy and entropy. (b, c, d) Boxplots for some drug-like properties of the selected Cz inhibitors with favorable and unfavorable entropy, and favorable enthalpy contribution. (b) SLogP = calculated logarithm of the partition coefficient in octanol, (c) ExactMW = molecular mass (Da) and (d) TPSA = topological polar surface area (Å²). Classes **De** and **Fe** are for the statistical binary classification as detrimental entropy (**De**) and favorable entropy (**Fe**), respectively.

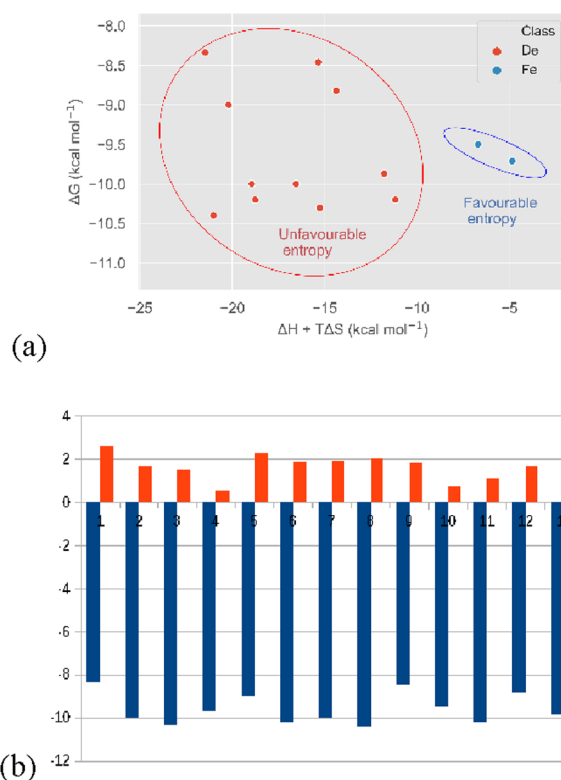


Fig. 15. ITC representation of favorable vs unfavorable entropy. (a) ITC data for the favorable enthalpic contribution of Cz inhibitors with favorable (compounds **10g** and **4e** in the blue volume of the 95% confidence ellipsoid) and unfavorable entropy (ellipsoid in red) for the other inhibitors studied here; (b) Plot of the Enthalpy-Entropy Index ($I_E - E$): $(\Delta H + T\Delta S)/\Delta G$ ratio in red and ΔG in blue bars. Red bars **4** and **10** are for Cz inhibitors **4e** and **10g**, respectively. (For interpretation of the references to color in this figure legend, the reader is referred to the web version of this article.)

the change in enthalpy. The decrease in the enthalpy change contribution while improving the entropy change contribution may result from a loss in planarity, loss of the oxygen as a hydrogen bond acceptor and gain in flexibility to better accommodate the inhibitor in the active site.

On the contrary, the double transformation in P2 and P3 from **10a** to **10d** (Fig. 18) unfolds a strong subadditive effect in the free energy change which is driven mostly by a detrimental entropy contribution. Chemical substitution of the phenyl ring for the *tert*-butyl-*N*-methylpyrazole in P3 (**10a** → **10c**) increases the affinity towards Cz through a strong entropic effect which could be addressed to the desolvation process. However, for the same transformation in P3 (**10b** → **10d**), while having leucine in P2, we observed a detrimental entropy contribution trend that yields to an insignificant change in the net energy.

A similar observation occurs for transformation **10c** → **10d** when changing phenylalanine to leucine in P2. Nevertheless, both transformations **10a** → **10b** and **10a** → **10c** resulted in the gain of the entropic variation. To this end, we can define that *tert*-butyl-*N*-methylpyrazole in P3 increased the solubility of the inhibitor and formed positive interaction with the S3 region, as shown for CatL [27]. However, this double positive effect is achieved just if Phe in P2 is substituted with the less bulky and more flexible Leu.

3.2.1.1. Insight of single modification in P1 and P3 of Cz inhibitors by ITC. Recently [42], we evaluated the mechanistic reasons for the P1 modification in some dipeptidyl nitriles as Cz inhibitors, which resulted in an enthalpy inhibition process with a detrimental contribution from entropy. The inclusion of cyclopropane in carbon-1 of 2-aminoacetonitrile was a detrimental enthalpic change with favorable

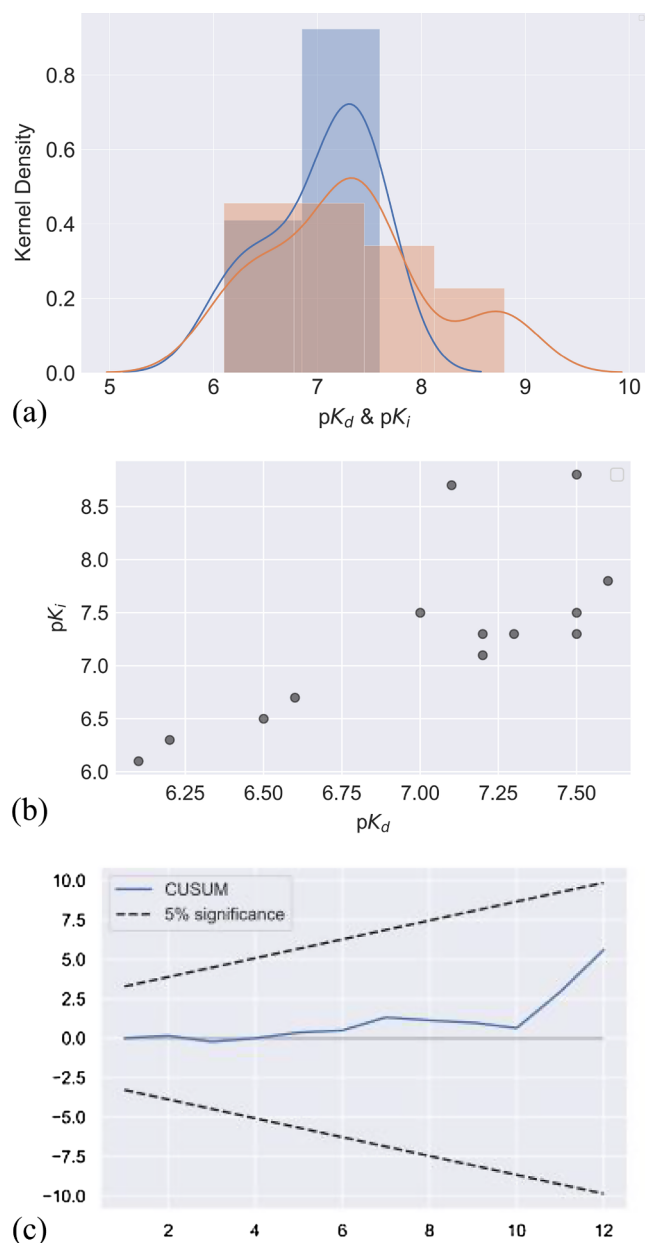


Fig. 16. (a) A plot with a kernel density estimates and histogram for pK_i (in blue) and pK_d (pink) data. (b) Scatter plot model of pK_i versus pK_d . Regression for data in (b) was obtained from the recursive RLS model whose stats are: $R^2 = 0.995$ for $pK_d = 1.0402 (\pm 0.022)$ with $z = 48.355$ and $P > |z| = 0.000$. The CUSUM statistic, the blue line in (c), does not expand outside the 5% significance bands. Models were run in python scripts. (For interpretation of the references to color in this figure legend, the reader is referred to the web version of this article.)

entropic change. Thus, in this work, we studied changes in P1 to better assess the role of other molecular fragments replacement. Structural modifications in P1 starting from compound **10c** display a clear trend: a strong positive effect in the entropic contributions (excluding **10e** and **10i**), which is balanced by a decrease in enthalpy (Fig. 19).

Inhibitors **10g**, **10h** and **10k** experienced almost complete EEC thanks to the specific modifications implemented. On the other hand, inhibitors **10e** and **10i** showed a decrease in binding energy. The **10g** and **10k** inhibitors are two special cases considering that the transformation resulted in the largest increase in the TPSA, from 99.81 Å² for **10c** to 112.7 Å² and 120.1 Å² to **10g** and **10k**, respectively.

To explain this trend, we can consider that the substitution of the

rigid cyclopropane in P1 leads to a greater degree of flexibility and subsite polar interaction. However, as already discussed [42], cyclopropane helps promote the Cys nucleophilic attack, by pointing the nitrile closer to the nucleophilic thiol.

Finally, we have studied the regiochemistry effect of the 5-phenylpyrimidine moiety in P3 when going from *para* (inhibitor **4e**) to *meta* (inhibitor **4c**), Fig. 20. The change in P3 shows a mild increase in binding affinity because of an improvement in enthalpy counterbalanced by detrimental enthalpy–entropy compensation. Molecular dynamics simulations (see 3.1) explains this phenomenon by considering an improvement of the interaction of the pyrimidine ring with Ser61 when it is in the *meta* position.

Due to solubility issues of some compounds we were not able to analyze the affinity by ITC. Therefore, we have used the Differential Scanning Calorimetry (DSC) method to quantify the thermal stability of Cz in the apo form and with a series of inhibitors (see 3.3).

3.3. DSC analysis

Experimental results obtained for Cz in the *apo* form and when incubated with 13 compounds by differential scanning calorimetry (DSC) are reported in Table 6.

First, a reversibility study of the thermal unfolding of Cz was performed, seeking to identify if the process of unfolding was reversible or irreversible. The result obtained is shown in Fig. 21.

By the sequential scans, it was determined that Cz has an irreversible unfolding due to the non-appearance of a peak in the second heating scan. This result is in agreement with previous studies made for papain and other CPs of this family [43].

Having established the irreversible unfolding of the protein, the assay of the native protein was carried out to determine its temperature of melting (T_m) (see SI chapter S4). The presence of one peak is indicative of the protein structure cooperativity. Cz has a two-domain structure and because only one peak appeared in the scan, both domains unfold cooperatively. A positive ΔC_p was observed for Cz with a mean value of approximately $+6.8 \text{ kcal mol}^{-1} \text{ K}^{-1}$. A positive ΔC_p indicates that the C_p of the unfolding state is greater than the folded state, which is mainly due to the exposure of hydrophobic amino acids to the solvent [44]. Calorimetric enthalpy (ΔH^{cal}) was obtained by integrating the area under the peak before the baseline subtraction (see Fig. S13); the value corresponds to the enthalpy at the T_m . The ΔH^{cal} consists of endothermic and exothermic contributions correlated to the bonds and interactions disrupted by the heating process. The Van't Hoff enthalpy (ΔH^{VH}) was achieved when the fit of the raw data was done using a two-state scaled model equation. This equation considers the equilibrium constant (K_{eq}), which takes both states of the protein in perfect equilibrium.

The ratio $\Delta H^{\text{cal}} / \Delta H^{\text{VH}}$ of the enthalpies was obtained aiming to identify if the unfolding process of Cz follows a two-state model, without the formation of intermediates. As shown in Table 6, the ratio $\Delta H^{\text{cal}} / \Delta H^{\text{VH}}$ is very close to 1.0 and the standard deviation of the analysis indicates that both enthalpies can be equal, and the process of unfolding can be considered of two states with an equilibrium constant equal to 1. So, as the enthalpy values are close, a thermal unfolding without the presence of intermediates was considered for Cz [45]. Afterwards, the analysis proceeded to the investigation of the thermal unfolding of Cz in the presence of different ligands (Table 6).

The T_m values are higher than that obtained for the native protein, showing that the ligands are interacting with the folded protein, thus stabilizing the Cz structure. The positive shift indicates that the equilibrium constant was displaced to the folded form due to the stabilization of the Cz structure. Because of that, when Cz is bound to the ligands the thermal unfolding probably occurred through the presence of an intermediate and the two domains may unfold separately but not independently as only one peak was observed.

In general, ΔT_m is in good agreement with the pK_i values. However,

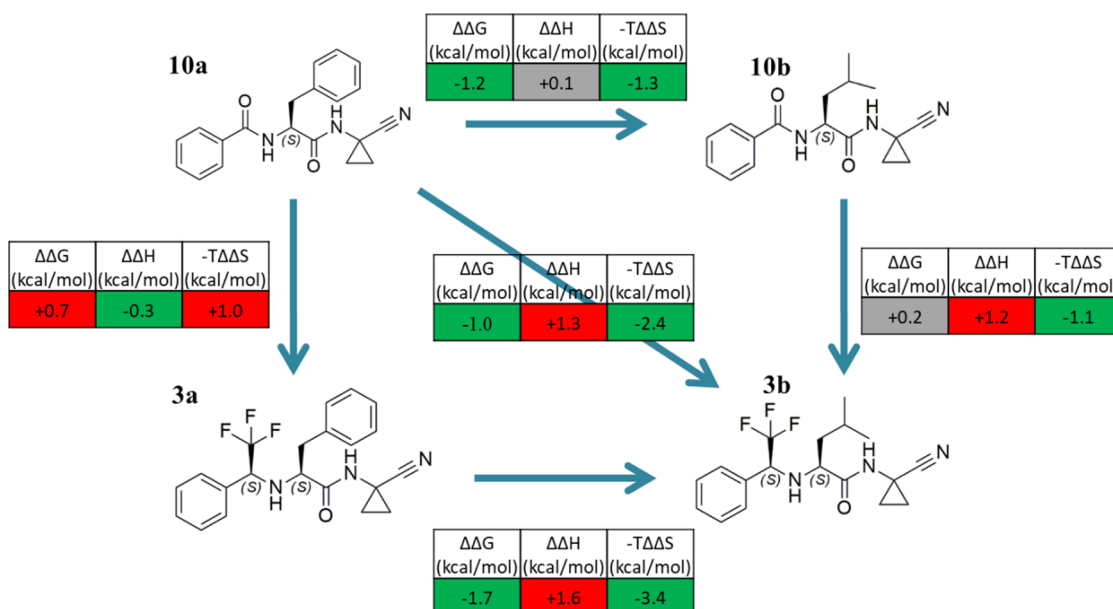


Fig. 17. Thermodynamic cycle analysis from compound **10a** to **3b**. The thermodynamics differences $\Delta\Delta X_{n \rightarrow m} = \Delta X_m - \Delta X_n$ ($X = G, H, S$ for the transformations $[n \rightarrow m]$) are color-coded as red (negative), green (positive), grey (no significant difference $\Delta < 0.2$). The values were calculated from the data in Table 5. (For interpretation of the references to color in this figure legend, the reader is referred to the web version of this article.)

because most of the ligands have pK_i between 7.0 and 8.0, the ΔT_m did not change significantly (median of 10.5, $se = 0.484$, $sd = 1.74$, variance = 3.04, range 6.1–13.5).

The most potent ligand in the series, **3c**, whose Cz affinity (pK_i) is 8.7 was able to thermally stabilize the Cz structure with 13.5 °C. On the other hand, **10a** ($pK_i = 6.7$) displayed one of the lowest ΔT_m of the series. These findings suggest that the DSC analysis can be used to estimate affinity in the presence of a broad SAR. It is worth noting that compound **10d** has the second-highest ΔT_m , with a pK_i 1.5 lower than **3c**, nonetheless both displayed the highest enthalpy contribution in the binding process (see chapter 3.2).

4. Conclusion

As we have heretofore observed, the literature is full of small molecule inhibitors of a single CP while little is known about cross-class inhibitors amongst mammalian and protozoa CPs [1]. This work aims to unveil new high-affinity non-peptide inhibitors of protozoan CPs (Cz and LmCPB), which in turn can be mammalian CPs (CatK, CatL, CatS) high-affinity inhibitors by unique structural modifications. We have performed an MMP/SAR analysis which revealed that Leu in P2 and (S)-benzyl moiety in P1 are privileged structures for the design of new cross-class inhibitors. Among several high-affinity CP inhibitors, compound **3c**, which exhibits the single-digit nanomolar K_i value (2 nM that yields a $pK_i \sim 8.7$) for all five studied CPs, was subsequently investigated through a double SAR cycle. The bioisosteric replacement of

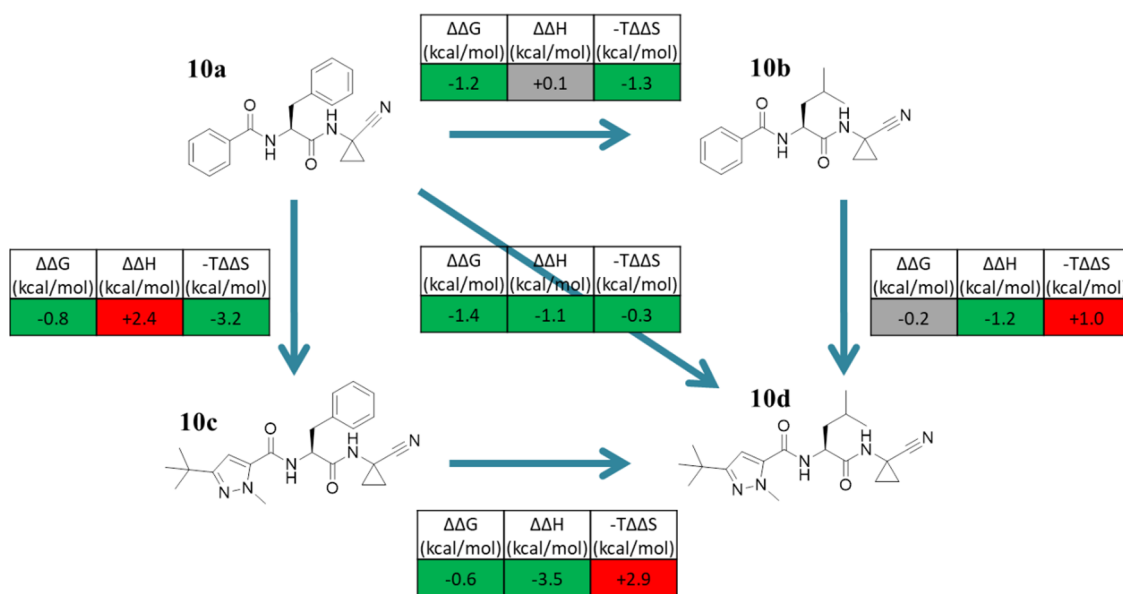


Fig. 18. Thermodynamic cycle analysis for **10a** transformations to yield **10d**. The thermodynamics differences $\Delta\Delta X_{n \rightarrow m} = \Delta X_m - \Delta X_n$ ($X = G, H, S$ for the transformations $[n \rightarrow m]$) are color-coded as red (negative), green (positive), grey (no significant difference $\Delta < 0.2$). The values were calculated from the data in Table 5. (For interpretation of the references to color in this figure legend, the reader is referred to the web version of this article.)

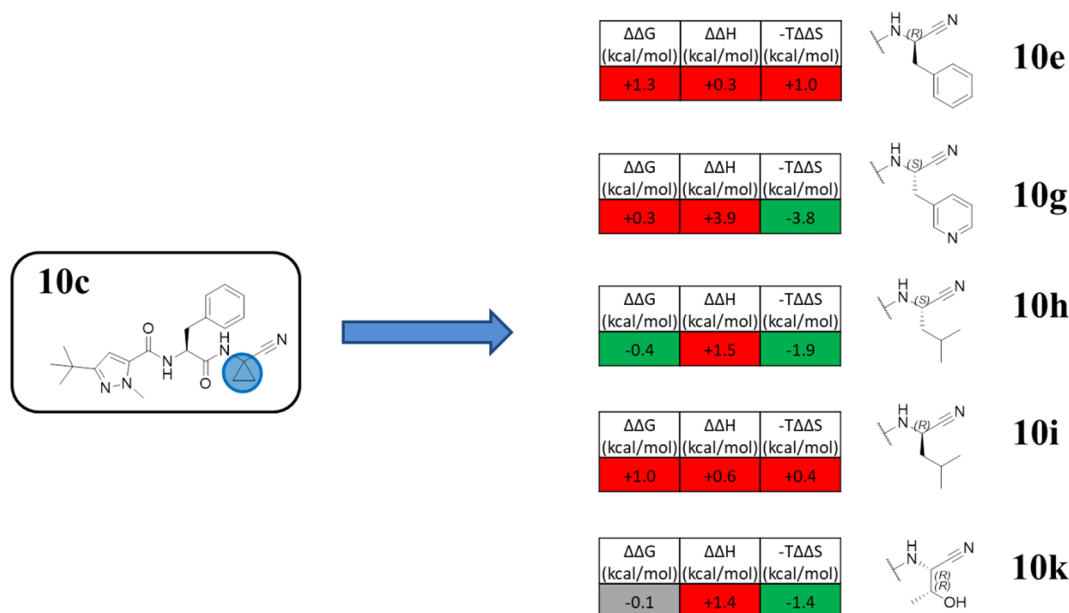


Fig. 19. Thermodynamic MMP analysis of P1 modification for compound **10c**. The thermodynamics differences $\Delta\Delta X_{n \rightarrow m} = \Delta X_m - \Delta X_n$ (X = G, H, S for the transformations [n → m]) are color-coded as red (negative), green (positive), grey (no significant difference $\Delta < 0.2$). The values were calculated from the data in Table 5. (For interpretation of the references to color in this figure legend, the reader is referred to the web version of this article.)

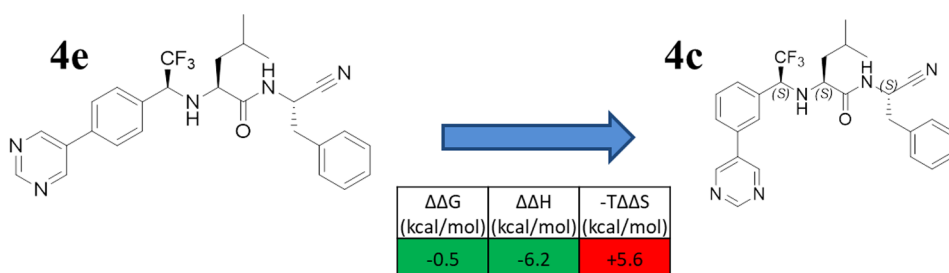


Fig. 20. Thermodynamic MMP analysis of **4e** vs **4c**. The thermodynamics differences $\Delta\Delta X_{n \rightarrow m} = \Delta X_m - \Delta X_n$ (X = G, H, S for the transformations [n → m]) are color-coded as red (negative), green (positive), grey (no significant difference $\Delta < 0.2$). The values were calculated from the data in Table 5. (For interpretation of the references to color in this figure legend, the reader is referred to the web version of this article.)

Table 6

Experimental results obtained for 13 compounds when incubated with Cz and analyzed by differential scanning calorimetry (DSC). The ΔT_m was obtained by subtracting the T_m of the incubated protein by the T_m of the native protein. The conditions for the assays were the same used for native cruzain assays with the only difference being the presence of the ligands. The mean values of the two measurements are presented. T_m = midpoint thermal unfolding (also melting temperature), ΔH^{cal} = calorimetric enthalpy, ΔH^{VH} = Van't Hoff enthalpy.

Ligand	T_m (°C)	ΔT_m (°C)	ΔH^{cal} (kcal mol ⁻¹)	ΔH^{VH} (kcal mol ⁻¹)	$\Delta H^{cal}/\Delta H^{VH}$
Apo-Cz	66.4 ± 0.1	–	100 ± 5	113 ± 12	0.9
3c	79.7	13.5	127 ± 15	187 ± 2	0.7
4a	76.5	10.5	170 ± 8	159 ± 3	1
4b	76.7	10.7	152 ± 2.8	168 ± 1.99	0.9
10a	72.5	6.1	115 ± 2	133 ± 2	0.8
10b	76.4	10.2	107 ± 6	193 ± 12	0.5
10b	76.9	10.7	128 ± 28	191 ± 12	0.7
10c	76.7	10.5	105 ± 6	189 ± 13	0.5
10d	79.3	13.1	117 ± 2	196 ± 7	0.6
10f	76.2	10.0	75 ± 2	198 ± 12	0.4
10g	76.6	10.4	74 ± 3	188 ± 9	0.4
10h	76.8	10.6	88 ± 2	202 ± 12	0.4
10j	77.1	10.9	125 ± 13	178 ± 11	0.7
10k	75.8	9.6	77 ± 5	212 ± 15	0.4

the carbonyl group in P2/P3 for the CF₃ group and the presence of Leu in the P2 position had a superadditive effect on affinity for all the CPs. Likewise, if from one side the *para* biphenyl in P3 is a privileged structure to gain selectivity amid protozoan and mammalian CPs, *meta*

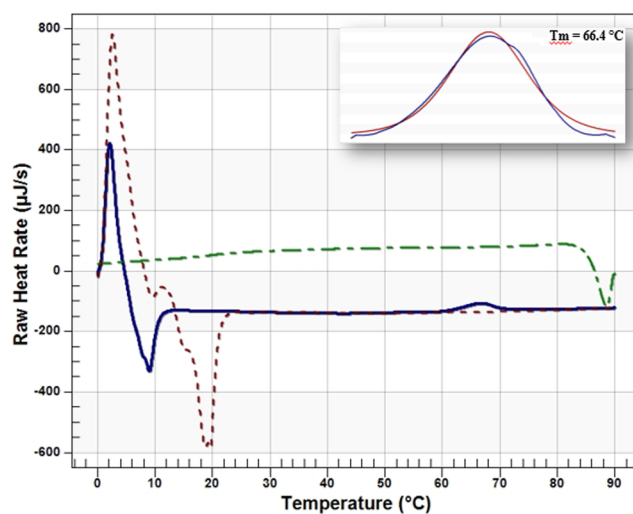


Fig. 21. Reversibility assay performed for Cz. The blue line corresponds to the first heating scan, ranging from 0 to 90 °C, the green line corresponds to the cooling scan and the red line to the second heating process. The peak of the unfolding process is depicted with $T_m = 66.4$ °C. The scans were done at 3 atm and with a rate of 2 °C per minute. (For interpretation of the references to color in this figure legend, the reader is referred to the web version of this article.)

phenyl substituent led to high-affinity cross-class inhibitors of different CPs such as compounds **3e** and **4c**. Besides that, molecular dynamics simulations for Cz reveal two possible modes of binding (MoB I and MoB II) for compounds **4a**, **4c**, **4d**, **4e** which could explain the strong nonadditivity SAR recently published [8].

The thermodynamic signatures for several compounds, obtained using ITC, display a strong enthalpy–entropy compensation which was surmounted by two compounds **10g** and **4e**. These compounds are the first cruzain inhibitors reported up to now to display a thermodynamic signature wherein both entropy and enthalpy favorably contribute to Gibbs binding energy. Finally, we also reported the first DSC analysis of Cz incubated with 13 different compounds where ΔT_m is in good agreement with the pK_i values spanning cruzain thermal stabilization from 6 to 13 °C.

In conclusion, this work is aimed at offering new insights into the optimization strategy for the design, synthesis, and biochemical/biophysical evaluation of potent cross-class CP inhibitors. This may ultimately aid advancing molecular designing efforts directed to reversible covalent inhibitors with direct implications for polypharmacology and multi-target screenings perhaps to include other cysteine endopeptidases.

Declaration of Competing Interest

The authors declare that they have no known competing financial interests or personal relationships that could have appeared to influence the work reported in this paper.

Acknowledgments

We are indebted to Fundação de Amparo à Pesquisa do Estado de São Paulo – FAPESP (grant #2013/18009-4, #2018/03985-1 and grant #2016/07946-5) for financing this project. Too, we would also like to thank the CAPES Drug Discovery program (Process #139/2015) that allowed us to evaluate LmCPB inhibitors. We want to acknowledge the National Council for Scientific and Technological Development (CNPq, grant # 304030/2018-0) in Brazil for scholarships.

Appendix A. Supplementary data

Supplementary data to this article can be found online at <https://doi.org/10.1016/j.bioorg.2020.104039>.

References

- [1] L. Cianni, C.W. Feldmann, E. Gilberg, M. Gütschow, L. Juliano, A. Leitão, J. Bajorath, C.A. Montanari, Can Cysteine Protease Cross-Class Inhibitors Achieve Selectivity? *J. Med. Chem.* (2019), <https://doi.org/10.1021/acs.jmedchem.9b00683>.
- [2] L. Kramer, D. Turk, B. Turk, The Future of Cysteine Cathepsins in Disease Management, *Trends Pharmacol. Sci.* 38 (2017) 873–898, <https://doi.org/10.1016/j.tips.2017.06.003>.
- [3] M. Sajid, S.A. Robertson, L.S. Brinen, J.H. McKerrow, Cruzain : the path from target validation to the clinic, *Adv. Exp. Med. Biol.* 712 (2011) 100–115, https://doi.org/10.1007/978-1-4419-8414-2_7.
- [4] P.-A. Casgrain, C. Martel, W.R. McMaster, J.C. Mottram, M. Olivier, A. Descoteaux, Cysteine Peptidase B Regulates Leishmania mexicana Virulence through the Modulation of GP63 Expression, *PLoS Pathog.* 12 (2016) e1005658, <https://doi.org/10.1371/journal.ppat.1005658>.
- [5] D.N. Deaton, S. Kumar, Cathepsin K Inhibitors: Their Potential as Anti-Osteoporosis Agents, in: *Progress in Medicinal Chemistry*, Elsevier, 2004: pp. 245–375. [https://doi.org/10.1016/S0079-6468\(04\)42006-2](https://doi.org/10.1016/S0079-6468(04)42006-2).
- [6] J.R. Coura, P.A. Viñas, Chagas disease: a new worldwide challenge, *Nature* 465 (2010) S6–S7, <https://doi.org/10.1038/nature09221>.
- [7] L. Cianni, C. Lemke, E. Gilberg, C. Feldmann, F. Rosini, F.D.R. Rocho, J.F.R. Ribeiro, D.Y. Tezuka, C.D. Lopes, S. de Albuquerque, J. Bajorath, S. Laufer, A. Leitão, M. Gütschow, C.A. Montanari, I.C. Almeida, Mapping the S1 and S1' subsites of cysteine proteases with new dipeptidyl nitrile inhibitors as trypanocidal agents, *PLoS Negl Trop Dis* 14 (2020) e0007755, <https://doi.org/10.1371/journal.pntd.0007755>.
- [8] J.C. Gomes, L. Cianni, J. Ribeiro, F. dos Reis Rocho, S. da Costa Martins, P.H.J. Silva, C.B. Batista, C.H. Moraes, L.H.G. Franco, P.W. Freitas-Junior, A. Kenny, A.C.B. Leitão, D. de Burtoloso, C.A.M. Vita, Synthesis and structure-activity relationship of nitrile-based cruzain inhibitors incorporating a trifluoroethylamine-based P2 amide replacement, *Bioorg. Med. Chem.* 27 (2019) 115083, <https://doi.org/10.1016/j.bmc.2019.115083>.
- [9] L.A.A. Avelar, C.D. Camilo, S. de Albuquerque, W.B. Fernandes, C. Gonçalves, P.W. Kenny, A. Leitão, J.H. McKerrow, C.A. Montanari, E.V.M. Orozco, J.F.R. Ribeiro, J.R. Rocha, F. Rosini, M.E. Saidel, Molecular Design, Synthesis and Trypanocidal Activity of Dipeptidyl Nitriles as Cruzain Inhibitors, *PLoS Negl Trop Dis.* 9 (2015) e0003916, <https://doi.org/10.1371/journal.pntd.0003916>.
- [10] A.C.B. Burtoloso, S. de Albuquerque, M. Furber, J.C. Gomes, C. Gonçalves, P.W. Kenny, A. Leitão, C.A. Montanari, J.C. Quilès, J.F.R. Ribeiro, J.R. Rocha, Anti-trypanosomal activity of non-peptidic nitrile-based cysteine protease inhibitors, *PLoS Negl Trop Dis.* 11 (2017) e0005343, <https://doi.org/10.1371/journal.pntd.0005343>.
- [11] J.Y. Gauthier, N. Chauret, W. Cromlish, S. Desmarais, L.T. Duong, J.-P. Falgout, D.B. Kimmel, S. Lamontagne, S. Léger, T. LeRiche, C.S. Li, F. Massé, D.J. McKay, D.A. Nicoll-Griffith, R.M. Oballa, J.T. Palmer, M.D. Percival, D. Riendeau, J. Robichaud, G.A. Rodan, S.B. Rodan, C. Seto, M. Thérien, V.-L. Truong, M.C. Venuti, G. Wesolowski, R.N. Young, R. Zamboni, W.C. Black, The discovery of odanacatib (MK-0822), a selective inhibitor of cathepsin K, *Bioorg. Med. Chem. Lett.* 18 (2008) 923–928, <https://doi.org/10.1016/j.bmcl.2007.12.047>.
- [12] J. Lameira, V. Bonatto, L. Cianni, F. dos Reis Rocho, A. Leitão, C.A. Montanari, Predicting the affinity of halogenated reversible covalent inhibitors through relative binding free energy, *Phys. Chem. Chem. Phys.* 21 (2019) 24723–24730, <https://doi.org/10.1039/C9CP04820K>.
- [13] L. Cianni, G. Sartori, F. Rosini, D.V. De, G. Pires, B.R. Lopes, A. Leitão, A.C.B. Burtoloso, C.A. Montanari, Leveraging the cruzain S3 subsite to increase affinity for reversible covalent inhibitors, *Bioorg. Chem.* 79 (2018) 285–292, <https://doi.org/10.1016/j.bioorg.2018.04.006>.
- [14] J. Cai, J. Robinson, S. Belshaw, K. Everett, X. Fradera, M. van Zeeland, L. van Berkum, P. van Rijsbergen, L. Popplestone, M. Baugh, M. Dempster, J. Bruin, W. Hamilton, E. Kinghorn, P. Westwood, J. Kerr, Z. Rankovic, W. Arbuckle, D.J. Bennett, P.S. Jones, C. Long, I. Martin, J.C.M. Uitdehaag, T. Meulemans, Trifluoromethylphenyl as P2 for ketoamide-based cathepsin S inhibitors, *Bioorg. Med. Chem. Lett.* 20 (2010) 6890–6894, <https://doi.org/10.1016/j.bmcl.2010.10.012>.
- [15] B.T. Mott, R.S. Ferreira, A. Simeonov, A. Jadhav, K.-K.-H. Ang, W. Leister, M. Shen, J.T. Silveira, P.S. Doyle, M.R. Arkin, J.H. McKerrow, J. Inglese, C.P. Austin, C.J. Thomas, B.K. Shoichet, D.J. Maloney, Identification and Optimization of Inhibitors of Trypanosomal Cysteine Proteases: Cruzain, Rhodesain, and TbCatB, *J. Med. Chem.* 53 (2010) 52–60, <https://doi.org/10.1021/jm901069a>.
- [16] A. Jakalian, D.B. Jack, C.I. Bayly, Fast efficient generation of high-quality atomic charges. AM1-BCC model: II. Parameterization and validation, *J. Comput. Chem.* 23 (2002) 1623–1641, <https://doi.org/10.1002/jcc.10128>.
- [17] W.L. Jorgensen, J. Chandrasekhar, J.D. Madura, R.W. Impey, M.L. Klein, Comparison of simple potential functions for simulating liquid water, *J. Chem. Phys.* 79 (1983) 926–935, <https://doi.org/10.1063/1.445869>.
- [18] D.A. Case, T.E. Cheatham, T. Darden, H. Gohlke, R. Luo, K.M. Merz, A. Onufriev, C. Simmerling, B. Wang, R.J. Woods, The Amber biomolecular simulation programs, *J. Comput. Chem.* 26 (2005) 1668–1688, <https://doi.org/10.1002/jcc.20290>.
- [19] J.A. Maier, C. Martinez, K. Kasavajhala, L. Wickstrom, K.E. Hauser, C. Simmerling, ffl4SB: Improving the Accuracy of Protein Side Chain and Backbone Parameters from ff99SB, *J. Chem. Theory Comput.* 11 (2015) 3696–3713, <https://doi.org/10.1021/acs.jctc.5b00255>.
- [20] H.C. Andersen, Rattle: A “velocity” version of the shake algorithm for molecular dynamics calculations, *J. Comput. Phys.* 52 (1983) 24–34, [https://doi.org/10.1016/0021-9991\(83\)90014-1](https://doi.org/10.1016/0021-9991(83)90014-1).
- [21] D.R. Roe, I.I. Thomas, E. Cheatham, PTRAJ and CPPTRAJ: Software for Processing and Analysis of Molecular, Dynamics Trajectory Data (2013), <https://doi.org/10.1021/ct400341p>.
- [22] Gnuplot: An Interactive Plotting Program, (n.d.). <http://www.gnuplot.info/docs/4.0/gnuplot.html> (accessed April 27, 2020).
- [23] E.F. Pettersen, T.D. Goddard, C.C. Huang, G.S. Couch, D.M. Greenblatt, E.C. Meng, T.E. Ferrin, UCSF Chimera—A visualization system for exploratory research and analysis, *J. Comput. Chem.* 25 (2004) 1605–1612, <https://doi.org/10.1002/jcc.20084>.
- [24] L. Cianni, C. Lemke, E. Gilberg, C. Feldmann, F. Rosini, F. dos Reis Rocho, J.F.R. Ribeiro, D.Y. Tezuka, C.D. Lopes, S. de Albuquerque, J. Bajorath, S. Laufer, A. Leitão, M. Gütschow, C.A. Montanari, Mapping the S1 and S1' subsites of cysteine proteases with new dipeptidyl nitrile inhibitors as trypanocidal agents, *BioRxiv.* (2019) 760736, <https://doi.org/10.1101/760736>.
- [25] Enzyme Database - BRENDA, (n.d.). <https://www.brenda-enzymes.org/> (accessed April 27, 2020).
- [26] C. Tyrchan, E. Evertsson, Matched Molecular Pair Analysis in Short: Algorithms, Applications and Limitations, *Comput. Struct. Biotechnol. J.* 15 (2017) 86–90, <https://doi.org/10.1016/j.csbj.2016.12.003>.
- [27] N. Asaad, P.A. Bethel, M.D. Coulson, G.E. Dawson, S.J. Ford, S. Gerhardt, M. Grist, G.A. Hamlin, M.J. James, E.V. Jones, G.I. Karoutchi, P.W. Kenny, A.D. Morley, K. Oldham, N. Rankine, D. Ryan, S.L. Wells, L. Wood, M. Augustin, S. Krapp, H. Simader, S. Steinbacher, Dipeptidyl nitrile inhibitors of Cathepsin L, *Bioorg. Med. Chem. Lett.* 19 (2009) 4280–4283, <https://doi.org/10.1016/j.bmcl.2009.05.071>.
- [28] P.K. Jadhav, M.A. Schiffler, K. Gavardinas, E.J. Kim, D.P. Matthews, M.A. Staszak, D.S. Coffey, B.W. Shaw, K.C. Cassidy, R.A. Brier, Y. Zhang, R.M. Christie,

- W.F. Matter, K. Qing, J.D. Durbin, Y. Wang, G.G. Deng, Discovery of Cathepsin S Inhibitor LY3000328 for the Treatment of Abdominal Aortic Aneurysm, *ACS Med. Chem. Lett.* 5 (2014) 1138–1142, <https://doi.org/10.1021/ml500283g>.
- [29] L.A.A. Avelar, C.D. Camilo, S. de Albuquerque, W.B. Fernandes, C. Gonçalves, P.W. Kenny, A. Leitão, J.H. McKerrow, C.A. Montanari, E.V.M. Orozco, J.F.R. Ribeiro, J.R. Rocha, F. Rosini, M.E. Saidel, Molecular Design Synthesis and Trypanocidal Activity of Dipeptidyl Nitriles as Cruzain Inhibitors, *PLOS Negl. Trop. Dis.* 9 (2015) e0003916, <https://doi.org/10.1371/journal.pntd.0003916>.
- [30] D. Stumpfe, J. Bajorath, Exploring Activity Cliffs in Medicinal Chemistry: Miniperspective, *J. Med. Chem.* 55 (2012) 2932–2942, <https://doi.org/10.1021/jm201706b>.
- [31] C. Kramer, J.E. Fuchs, K.R. Liedl, Strong Nonadditivity as a Key Structure-Activity Relationship Feature: Distinguishing Structural Changes from Assay Artifacts, *J. Chem. Inf. Model.* 55 (2015) 483–494, <https://doi.org/10.1021/acs.jcim.5b00018>.
- [32] I.M. Prokopczyk, J.F. Ribeiro, G.R. Sartori, R. Sesti-Costa, J.S. Silva, R.F. Freitas, A. Leitão, C.A. Montanari, Integration of methods in cheminformatics and biocalorimetry for the design of trypanosomatid enzyme inhibitors, *Future Med. Chem.* 6 (2014) 17–33, <https://doi.org/10.4155/fmc.13.185>.
- [33] G. Calabrò, C.J. Woods, F. Powlesland, A.S.J.S. Mey, A.J. Mulholland, J. Michel, Elucidation of Nonadditive Effects in Protein-Ligand Binding Energies: Thrombin as a Case Study, *J. Phys. Chem. B.* 120 (2016) 5340–5350, <https://doi.org/10.1021/acs.jpcc.6b03296>.
- [34] O.A. Khakhel, T.P. Romashko, Extrathermodynamics: Varieties of Compensation Effect, *J. Phys. Chem. A.* 120 (2016) 2035–2040, <https://doi.org/10.1021/acs.jpca.6b00493>.
- [35] G. Williams, G.G. Ferenczy, J. Ulander, G.M. Keserü, Binding thermodynamics discriminates fragments from druglike compounds: a thermodynamic description of fragment-based drug discovery, *Drug Discov. Today.* 22 (2017) 681–689, <https://doi.org/10.1016/j.drudis.2016.11.019>.
- [36] A. Gaulton, A. Hersey, M. Nowotka, A.P. Bento, J. Chambers, D. Mendez, P. Mutowo, F. Atkinson, L.J. Bellis, E. Cibrián-Uhalte, M. Davies, N. Dedman, A. Karlsson, M.P. Magariños, J.P. Overington, G. Papadatos, I. Smit, A.R. Leach, The ChEMBL database in 2017, *Nucleic Acids Res.* 45 (2017) D945–D954, <https://doi.org/10.1093/nar/gkw1074>.
- [37] E. Freire, Do enthalpy and entropy distinguish first in class from best in class? *Drug Discov. Today.* 13 (2008) 869–874, <https://doi.org/10.1016/j.drudis.2008.07.005>.
- [38] Y. Li, Z. Zhang, Q. Feng, D. Yi, F. Lu, An efficacy evaluation method for non-normal outcomes in randomized controlled trials, *Sci. Rep.* 9 (2019) 11393, <https://doi.org/10.1038/s41598-019-47727-y>.
- [39] K.J. Åström, B. Wittenmark, *Computer-controlled systems: theory and design*, 3rd ed, Prentice Hall, Upper Saddle River, N.J., 1997.
- [40] E. Ronchetti, C. Field, W. Blanchard, Robust Linear Model Selection by Cross-Validation, *J. Am. Stat. Assoc.* 92 (1997) 1017–1023, <https://doi.org/10.1080/01621459.1997.10474057>.
- [41] O.A. Grigg, V.T. Farewell, D.J. Spiegelhalter, Use of risk-adjusted CUSUM and RSPRT charts for monitoring in medical contexts, *Stat. Methods Med. Res.* 12 (2003) 147–170, <https://doi.org/10.1177/096228020301200205>.
- [42] A.M. Dos Santos, L. Cianni, D. De Vita, F. Rosini, A. Leitão, C.A. Laughton, J. Lameira, C.A. Montanari, Experimental study and computational modelling of cruzain cysteine protease inhibition by dipeptidyl nitriles, *Phys. Chem. Chem. Phys.* 20 (2018) 24317–24328, <https://doi.org/10.1039/C8CP03320J>.
- [43] S. Solís-Mendiola, A. Rojo-Domínguez, A. Hernández-Arana, Cooperativity in the unfolding transitions of cysteine proteinases. Calorimetric study of the heat denaturation of chymopapain and papain, *Biochimica et Biophysica, Acta (BBA) - Protein Struct. Mol. Enzymol.* 1203 (1993) 121–125, [https://doi.org/10.1016/0167-4838\(93\)90045-S](https://doi.org/10.1016/0167-4838(93)90045-S).
- [44] N.V. Prabhu, K.A. Sharp, HEAT CAPACITY IN PROTEINS, *Annu. Rev. Phys. Chem.* 56 (2005) 521–548, <https://doi.org/10.1146/annurev.physchem.56.092503.141202>.
- [45] G. Bruylants, J. Wouters, C. Michaux, Differential Scanning Calorimetry in Life Science: Thermodynamics, Stability, Molecular Recognition and Application in Drug Design, *CMC* 12 (2005) 2011–2020, <https://doi.org/10.2174/0929867054546564>.